ExaQUte

Exascale Quantification of Uncertainties for Technology and Science Simulation

D7.4 Final report on Stochastic Optimization results

Document information table

Contract number:	800898
Project acronym:	ExaQUte
Project Coordinator:	CIMNE
Document Responsible Partner:	str.ucture
Deliverable Type:	REPORT
Dissemination Level:	Confidential
Related WP & Task:	WP6, Task 6.4; WP7, Task 7.5 & 7.7
Status:	Internal revision

Authoring

Prepared by:				
Authors	Partner	Modified Page/Sections	Version	Comments
Sami Bidier	str.ucture	1, 4	1.0	
Ustim Khristenko	TUM	2	1.0	
Anoop Kodakkal	TUM	3	1.0	

Change Log

Versions	Modified Page/Sections	Comments
V1.0	First version	

Approval

Approved by:				
	Name	Partner	Date	OK
Task leader		TUM		✓
WP leader	Alexander Michalski	str.ucture	23.11.21	✓
Coordinator	Riccardo Rossi	CIMNE		✓

Executive summary

This deliverable report focuses on the final stochastic optimization results obtained within the EXAscale Quantification of Uncertainties for Technology and Science Simulation (ExaQUte) project. Details on a novel wind inlet generator that is able to incorporate local wind-field data through a deep-learned rapid distortion model and generates the turbulent wind data during run-time is presented in section 2. Section 3 presents the results of the overall stochastic optimization procedure applied to a twisted tapered tower with multiple design parameters within an uncertain synthetic wind field. Thereby, the significance of the developed methods and the obtained results are discussed and their integration in industrial wind-engineering workflows is outlined in section 4.

Contents

List of Figures

Nomenclature / Acronym list

Acronym	Meaning
CFD	Computational Fluid Dynamics
CVaR	Conditional Value at Risk
CWE	Computational Wind Engineering
ExaQUte	Exascale Quantification of Uncertainties for Technology and Science Simulation
DRD	Deep Rapid Distortion
OUU	Optimization under Uncertainties
PDE	Partial Differential Equation
QoI	Quantity of Ineterst
SFBL	shear-free Boundary Layer
SFPDE	stochastic fractional partial differential equation

1 Introduction

A building's outer skin does not only serve as the constructional and architectural hull, but is furthermore the first load-bearing element that is subjected to wind loads under varying and highly uncertain conditions. The designed building's orientation and geometry is often influenced by structural and architectural prerequisites and the principal design formalism in a very early stages of the planning process. Furthermore, latest trends in the construction industry point towards more slender and material-efficient buildings, slender high-rise buildings built from sustainable materials such as timber or recycled concrete and computer-aided prefabrication in quasi-modular structural elements. This leads to an increasingly complex and automated planning and construction process, where the aforementioned prerequisites and choices have an overwhelming impact on the structure, the construction process and materials, as well as the structural loads that the final building design needs to sustain due to wind loads.

Engineers and architects are therefore in need of tools, that offer a deep and precise understanding of how to optimize (a) the overall geometrical design while still taking numerous side conditions into account, but also (b) secondary load bearing elements, such as facades, in order to reduce wind load peaks on structural elements and guarantee a homogeneous load distribution and an efficient material design.

In this scope, the methods developed during the ExaQUte project with regard to stochastic optimization under uncertainties offer applicable tools for civil engineers to include shape optimization in the design process and offer Computational Wind Engineering (CEW) new well-defined tools to strengthen the integration of virtual wind tunnel testing into day to day investigations. The following sections give insight in the developed methods to include local wind data into CWE application by a data-driven approach and the showcase the overall stochastic optimization method on a high-rise building.

2 Data driven wind generation model

Our goal is to generate synthetic turbulent inlet conditions, which is an important application in computational fluid dynamics as a whole [56]. We choose to follow an established approach used in the wind engineering industry; see Andre et al. [2], Michalski et al. [49] and references therein. A contiguous section of spatially correlated turbulence is transformed into a stationary Gaussian process by identifying the x-component of the turbulent velocity field with a time axis via the transformation $x = U_{\mathrm{m}}t$. Here, $U_{\mathrm{m}} > 0$ is a mean velocity parameter which directly affects the spatial-to-temporal correlation of the synthetic turbulent inlet boundary conditions. Then, at each time step $t = t_k$, the turbulent velocity field $\mathbf{U}(\boldsymbol{x})|_{x=t_k/U_{\mathrm{m}}}$ is projected onto the inflow boundary of a numerical wind tunnel; see depiction in Figure 1. In this section, we discuss two approaches to construct the velocity field fluctuations fitting given statistical data. In Section 2.2, we present a turbulence model for a shear-free boundary layer (SFBL), constructed as a solution to a stochastic fractional partial differential equation (SFPDE) with imposed boundary conditions at the solid wall; see [37]. In Section 2.3, we present a data-driven nonlocal turbulence model for the atmospheric boundary layer in presence of uniform shear, which uses a neural network to simulate the eddy lifetime; see [38].

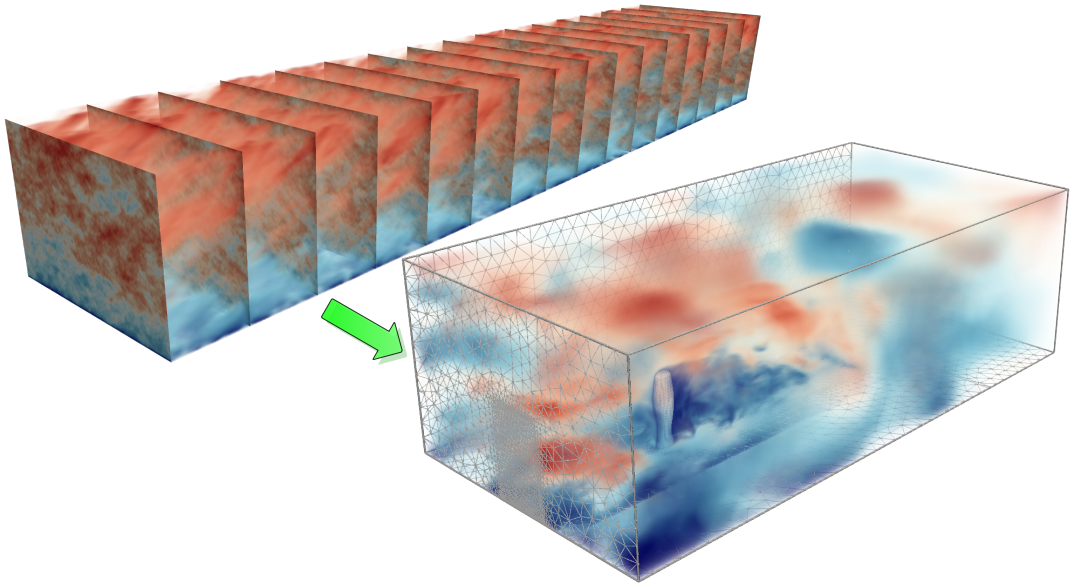

Figure 1: Inlet boundary conditions: projection of the wind onto the numerical wind tunnel inlet at each time step. Snapshots of synthetic wind, $\mathbf{U}(\boldsymbol{x}) = \langle \mathbf{U}(\boldsymbol{x}) \rangle + \mathbf{u}(\boldsymbol{x})$, mapped onto the inlet boundary in a numerical wind tunnel test of a modern high rise building. Turbulent inlet fluctuations $\mathbf{u}(\boldsymbol{x})$ are generated using Gaussian model. Then, the large eddy simulation was performed with the finite element software Kratos Multiphysics [19].

2.1 Synthetic wind velocity field fluctuation

We wish to model turbulent velocity fields $\mathbf{U}(\boldsymbol{x}) = \langle \mathbf{U}(\boldsymbol{x}) \rangle + \mathbf{u}(\boldsymbol{x}) \in \mathbb{R}^3$. Here, $\langle \mathbf{U} \rangle = (\langle U_1 \rangle, \langle U_2 \rangle, \langle U_3 \rangle)$ is the mean velocity field and $\mathbf{u} = (u_1, u_2, u_3)$ (sometimes also written (u, v, w)) are the zero-mean turbulent fluctuations. All of the models we choose to consider for $\mathbf{u}$ are *Gaussian*. That is, they are determined entirely from the two-point correlation tensor

$$R_{ij}(\boldsymbol{r}, \boldsymbol{x}, t) = \langle u_i(\boldsymbol{x}, t) u_j(\boldsymbol{x} + \boldsymbol{r}, t) \rangle.$$

When $R(\boldsymbol{r}, \boldsymbol{x}, t) = R(\boldsymbol{r}, t)$ depends only on the separation vector $\boldsymbol{r}$, the model is said to be spatially *homogeneous*. Alternatively, when $R(\boldsymbol{r}, \boldsymbol{x}, t) = R(\boldsymbol{r}, \boldsymbol{x})$ is independent of the time variable t, the model is said to be temporally *stationary*.

Frequently, it is convenient to consider the Fourier transform of the velocity field $\mathbf{u}$. In such cases, we express the field in terms of a generalized Fourier–Stieltjes integral,

$$\mathbf{u}(\boldsymbol{x}) = \int_{\mathbb{R}^3} \mathrm{e}^{\mathrm{i}\,\boldsymbol{k}\cdot\boldsymbol{x}} \, \mathrm{d}\boldsymbol{Z}(\boldsymbol{k}) \,, \tag{1}$$

where $\boldsymbol{Z}(\boldsymbol{k})$ is a three-component measure on $\mathbb{R}^3$, and $\boldsymbol{k} = (k_1, k_2, k_3)$ is the wavevector of magnitude $k = |\boldsymbol{k}|$ (wavenumber). The validity of this expression follows from the Wiener–Khinchin theorem [45]. Likewise, in the homogeneous setting, we may consider the Fourier transform of the covariance tensor, otherwise known as the *velocity-spectrum tensor*,

$$\Phi_{ij}(\boldsymbol{k}, t) = \frac{1}{(2\pi)^3} \int_{\mathbb{R}^3} \mathrm{e}^{-\mathrm{i}\,\boldsymbol{k}\cdot\boldsymbol{r}} \, R_{ij}(\boldsymbol{r}, t) \, \mathrm{d}\boldsymbol{r}.$$

Due to the cross-correlation theorem, the velocity-spectrum tensor can also be written

$$\Phi_{ij}(\boldsymbol{k}) = \langle \overline{\hat{u}}_i(\boldsymbol{k}) \hat{u}_j(\boldsymbol{k}) \rangle, \tag{2}$$

where $\hat{\mathbf{u}} = (\hat{u}_1, \hat{u}_2, \hat{u}_3)$ denotes the Fourier transform of $\mathbf{u}$.

Consider three-dimensional additive white Gaussian noise [24, 40] in the physical and frequency domains, denoted $\boldsymbol{\xi}(\boldsymbol{x})$ and $\hat{\boldsymbol{\xi}}(\boldsymbol{k})$, respectively, such that

$$\boldsymbol{\xi}(\boldsymbol{x}) = \int_{\mathbb{R}^3} \mathrm{e}^{\mathrm{i}\,\boldsymbol{k}\cdot\boldsymbol{x}}\, \hat{\boldsymbol{\xi}}(\boldsymbol{k})\, \mathrm{d}\boldsymbol{k} = \int_{\mathbb{R}^3} \mathrm{e}^{\mathrm{i}\,\boldsymbol{k}\cdot\boldsymbol{x}}\, \mathrm{d}\mathbf{W}(\boldsymbol{k}),$$

where $\boldsymbol{W}(\boldsymbol{k})$ is three-dimensional Brownian motion. We assume $\mathrm{d}\boldsymbol{Z}(\boldsymbol{k}) = G(\boldsymbol{k})\,\mathrm{d}\boldsymbol{W}(\boldsymbol{k}) = G(\boldsymbol{k})\hat{\boldsymbol{\xi}}(\boldsymbol{k})\,\mathrm{d}\boldsymbol{k}$, where $G(\boldsymbol{k})^* G(\boldsymbol{k}) = \Phi(\boldsymbol{k})$.

Let us begin with a standard form of the spectral tensor used in isotropic stationary and homogeneous turbulence models, namely,

$$\Phi_{ij}^{\mathrm{VK}}(\boldsymbol{k}) = (4\pi)^{-1} k^{-2} E(k) P_{ij}(\boldsymbol{k})\,. \tag{3}$$

Here, $E(k)$ is called the *energy spectrum function* and $P_{ij}(\boldsymbol{k}) = \delta_{ij} - \frac{k_i k_j}{k^2}$ is commonly referred to as the *projection tensor*. One common empirical model for $E(k)$, suggested by Von Karman [60], is given by the expression

$$E(k) = c_0^2\, \varepsilon^{2/3} k^{-5/3} \left(\frac{kL}{(1 + (kL)^2)^{1/2}} \right)^{17/3}. \tag{4}$$

Here, ε is the viscous dissipation of the turbulent kinetic energy, L is a length scale parameter, and $c_0^2 \approx 1.7$ is an empirical constant.

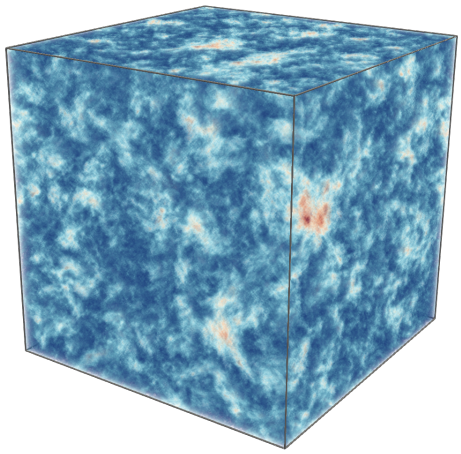

Figure 2: Example of Velocity field fluctuations: magnitude for a single realization of the random field

2.2 A fractional PDE model for turbulent velocity fields near solid walls

Recall that the Fourier transform of the scalar Laplacian is simply $-k^2$. Likewise, consider the Fourier transform $Q(\boldsymbol{k})$ of the curl operator, $\int_{\mathbb{R}^3} \nabla \times \boldsymbol{v}(\boldsymbol{r})\, \mathrm{e}^{-\mathrm{i}\,\boldsymbol{k}\cdot\boldsymbol{r}}\, \mathrm{d}\boldsymbol{r} = Q(\boldsymbol{k})\hat{\boldsymbol{v}}(\boldsymbol{k})$, where

$\hat{\boldsymbol{v}}(\boldsymbol{k}) = \int_{\mathbb{R}^3} \boldsymbol{v}(\boldsymbol{r})\, \mathrm{e}^{-\mathrm{i}\,\boldsymbol{k}\cdot\boldsymbol{r}}\, \mathrm{d}\boldsymbol{r}$. Observe that

$$Q(\boldsymbol{k}) = \mathrm{i} \begin{bmatrix} 0 & -k_3 & k_2 \\ k_3 & 0 & -k_1 \\ -k_2 & k_1 & 0 \end{bmatrix}$$

and, moreover, $P(\boldsymbol{k}) = k^{-2} Q(\boldsymbol{k})^* Q(\boldsymbol{k})$. Motivated by the decomposition $\Phi(\boldsymbol{k}) = G(\boldsymbol{k})^* G(\boldsymbol{k})$, we choose to simply write $G(\boldsymbol{k}) = \frac{1}{\sqrt{4\pi}} k^{-2} E^{1/2}(k) Q(\boldsymbol{k})$. Next, recalling $\mathrm{d}\boldsymbol{Z}(\boldsymbol{k}) = G(\boldsymbol{k})\, \mathrm{d}\boldsymbol{W}(\boldsymbol{k})$, it immediately follows that

$$\mathrm{d}\boldsymbol{Z}(\boldsymbol{k}) = Q(\boldsymbol{k}) \big(\frac{1}{\sqrt{4\pi} k^2} E^{1/2}(k)\, \mathrm{d}\boldsymbol{W}(\boldsymbol{k}) \big).$$

Integrating both sides with respect to $\boldsymbol{k}$, we arrive at the expression $\mathbf{u} = \nabla \times \boldsymbol{\psi}$, with a vector potential defined

$$\boldsymbol{\psi}(\boldsymbol{x}) = \frac{1}{\sqrt{4\pi}} \int_{\mathbb{R}^3} k^{-2} E^{1/2}(k)\, \mathrm{e}^{\mathrm{i}\,\boldsymbol{k}\cdot\boldsymbol{x}}\, \mathrm{d}\boldsymbol{W}(\boldsymbol{k})\,. \tag{5}$$

2.2.1 A fractional PDE for the velocity fluctuation field

We now proceed to relate the vector potential $\boldsymbol{\psi}(\boldsymbol{x})$ to the solution of a fractional PDE. Writing $\boldsymbol{\psi}(\boldsymbol{x}) = \int_{\mathbb{R}^3} \mathrm{e}^{\mathrm{i}\,\boldsymbol{k}\cdot\boldsymbol{x}}\, \mathrm{d}\boldsymbol{Y}(\boldsymbol{k})$, similar to eq. (1), and rearranging the factors in eq. (5), leads to

$$(1 + (kL)^2)^{17/12}\, \mathrm{d}\boldsymbol{Y}(\boldsymbol{k}) = c_0 \varepsilon^{1/3} L^{17/6}\, \mathrm{d}\boldsymbol{W}(\boldsymbol{k}).$$

Then, upon integrating both sides with respect to $\boldsymbol{k}$, we arrive at the fractional PDE

$$(I - L^2\Delta)^{17/12} \boldsymbol{\psi} = c_0 \varepsilon^{1/3} L^{17/6} \boldsymbol{\xi}. \tag{6}$$

This and all future differential equations are only properly understood in the sense of distributions, yet we continue to use the "strong form" for readability.

Let us denote by I the identity operator, $A = I - L^2\Delta$, $\mu = c_0 \varepsilon^{1/3}$, and $\alpha = 17/12$. With these symbols in hand, the derivation above can be summarized as follows:

$$\mathbf{u} = \nabla \times \boldsymbol{\psi}, \qquad \text{where} \quad A^\alpha \boldsymbol{\psi} = \mu L^{2\alpha} \boldsymbol{\xi}.$$

In the next section, we extend the simple FPDE model above in order to describe inhomogeneous turbulence on bounded domains. This is achieved by both generalizing the definition of the length scale L and the fractional operator A^α as well as introducing a physical notion of boundary conditions.

Equation (6) was derived from a very specific form of the energy spectrum function $E(k)$. Under the same decomposition of the spectral tensor $\Phi(\boldsymbol{x})$ given in eq. (3), a much more general family of homogeneous and stationary random field models derive from the following ansatz on the energy spectrum function:

$$k^{-4} E(\boldsymbol{k}) = \mu^2 \det(\bar{\boldsymbol{\Theta}})^{2/3\gamma} (1 + \boldsymbol{k}^\top \bar{\boldsymbol{\Theta}} \boldsymbol{k})^{-2\alpha_1} (\boldsymbol{k}^\top \bar{\boldsymbol{\Theta}} \boldsymbol{k})^{-2\alpha_2}. \tag{7}$$

Here, $\bar{\boldsymbol{\Theta}} \in \mathbb{R}^{3\times 3}$ is a fixed symmetric positive definite matrix and α_2, α_1, γ, and μ are additional scalar parameters.

Equation (7) is a broad generalization of eq. (4) which replaces E as function of $k = |\boldsymbol{k}|$ by E as function of $\boldsymbol{k}$. This flexibility allows us, for example, to consider anisotropic

effects. Indeed, just as L played the role of a length scale in eq. (4), here, $\bar{\boldsymbol{\Theta}}$ plays the role of a metric in Fourier space. In addition, observe that if $\bar{\boldsymbol{\Theta}} = L^2\mathsf{I}$, where I denotes the identity matrix, $4\alpha_2 = 4 - p_0$, $4\alpha_1 = 5/3 + p_0$, $\gamma = \alpha_1 + \alpha_2$, and $\mu^2 = C\varepsilon^{2/3}$, then eq. (7) reproduces the following common one-parameter homogeneous energy spectrum model [see, e.g., 52, p. 232]:

$$E(k) = C\varepsilon^{2/3}k^{-5/3}\left(\frac{kL}{((kL)^2+1)^{1/2}}\right)^{5/3+p_0}. \tag{8}$$

In this scenario, $p_0 = 4$ corresponds exactly to the von Kármán spectrum (4) considered previously; i.e., $\alpha_1 = \gamma = \frac{17}{12}$ and $\alpha_2 = 0$.

As in eq. (5), the vector potential $\boldsymbol{\psi}(\boldsymbol{x}) = \int \mathrm{e}^{\mathrm{i}\,\boldsymbol{k}\cdot\boldsymbol{x}}\,\mathrm{d}\boldsymbol{Y}(\boldsymbol{k})$ can also be written in terms of a Fourier–Stieltjes integral, weighted by $k^{-2}E^{1/2}(\boldsymbol{k})$. After rearranging factors, eq. (7) characterizes the vector potential $\boldsymbol{\psi}$ as the solution of the following fractional stochastic PDE on $\mathbb{R}^3$:

$$\big(I - \nabla\cdot(\bar{\boldsymbol{\Theta}}\nabla)\big)^{\alpha_1}\big(-\nabla\cdot(\bar{\boldsymbol{\Theta}}\nabla)\big)^{\alpha_2}\boldsymbol{\psi} = \mu\det(\bar{\boldsymbol{\Theta}})^{\gamma/3}\boldsymbol{\xi}. \tag{9}$$

Two immediate modifications of eq. (9) are now in order. First, we may replace the constant matrix $\bar{\boldsymbol{\Theta}}$ by a spatially varying metric tensor $\boldsymbol{\Theta}(\boldsymbol{x})$. This change immediately induces an inhomogeneous turbulence model. Second, we may consider substituting the white noise random variable $\boldsymbol{\xi}$ for a well-chosen colored noise variable denoted $\boldsymbol{\eta}$. Together, these two generalizations lead to a family of random field models written

$$\big(I - \nabla\cdot(\boldsymbol{\Theta}(\boldsymbol{x})\nabla)\big)^{\alpha_1}\big(-\nabla\cdot(\boldsymbol{\Theta}(\boldsymbol{x})\nabla)\big)^{\alpha_2}\boldsymbol{\psi} = \mu\det(\boldsymbol{\Theta}(\boldsymbol{x}))^{\gamma/3}\boldsymbol{\eta}. \tag{10}$$

Physically, the metric tensor $\boldsymbol{\Theta}(\boldsymbol{x})$ introduces inhomogeneous and anisotropic diffusion; this corresponds to local changes of the turbulence length scales which may result from complicated dynamics of interacting eddies. Statistically, it incorporates the possibility for spatially varying correlation lengths and also may contain distortion.

In order to motivate one possible choice of the stochastic forcing term $\boldsymbol{\eta}$, note that eq. (8) can adequately characterize both the energy-containing and inertial subranges, however, it fails in the dissipative range; namely, where k is large. In order to fit the dissipative range, one approach is to scale the energy spectrum with a decaying exponential function [see, e.g., 52, p. 233]:

$$E_\beta(k) = E(k)\,\mathrm{e}^{-\beta k},$$

where $\beta > 0$ is a positive constant, usually close to the Kolmogorov length scale. In the presence of shear, a different time-dependent modification is also natural to consider from the point of view of rapid distortion theory.

When α_2 and α_1 are chosen to match the energy spectrum model eq. (8), it is clear that $\alpha_2 + \alpha_1 = 17/12$ is independent of p_0. Under this constraint, α_2 mainly affect the behavior of the power spectrum at the origin and, likewise, the large scale structure of $\mathbf{u}$. In other words, the shape of the spectrum in the inertial subrange is unaffected by the precise choice of α_2 and $\alpha_1 = 17/12 - \alpha_2$; only the shape of the spectrum in the energy-containing range is affected (see Figure 3). An illustration of some energy spectra possibilities is included in Figure 3.

2.2.2 Boundary conditions

There are a number of different, equivalent, definitions of fractional operators on $\mathbb{R}^3$. However, moving from the free-space equation eq. (10) to a boundary value problem relies

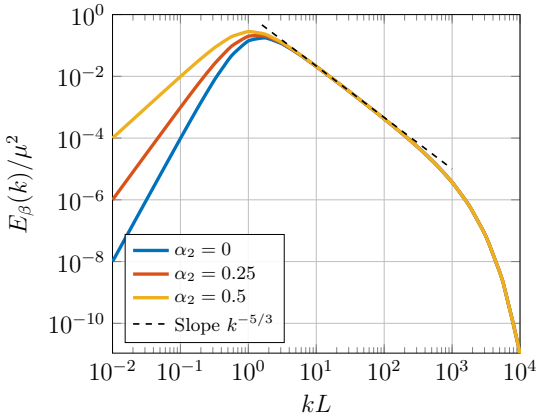

Figure 3: The energy spectrum $E_\beta(k)/\mu^2$ corresponding to (7) with $\bar{\boldsymbol{\Theta}} = L^2\mathsf{I}$. The sum $\alpha_2 + \alpha_1$ is fixed to 17/12, which guarantees the slope $k^{-5/3}$ in the inertial subrange. Different values of α_2 control the energy-containing range. And the exponent $\beta/L = 10^{-3}$ defines the exponential decay in the dissipative subrange.

on heuristics and can be done in a wide variety of ways; each of which may also differ by the specific definition of the fractional operator being used [44]. As stated previously, in this work, we choose to only deal with the spectral definition. In this setting, boundary conditions are applied to the corresponding integer-order operator and then incorporated implicitly by modifying the spectrum.

Assume that eq. (10) is posed on a three-dimensional simply-connected domain $\Omega \subsetneq \mathbb{R}^3$ with boundary $\Gamma = \partial\Omega$. We begin with the following heuristically chosen impermeability condition for the velocity field:

$$\mathbf{u} = \nabla\times\boldsymbol{\psi} \quad \text{in } \Omega, \qquad \mathbf{u}\cdot\boldsymbol{n} = 0 \quad \text{on } \Gamma. \tag{11}$$

Although more relaxed boundary conditions are also possible, we choose to enforce eq. (11) via a no-slip condition on the vector potential $\boldsymbol{\psi}$; specifically,

$$\boldsymbol{\psi} - (\boldsymbol{\psi}\cdot\boldsymbol{n})\boldsymbol{n} = \mathbf{0} \quad \text{on } \Gamma. \tag{12}$$

It turns out that eq. (12) is not enough to uniquely define $\boldsymbol{\psi}$ on Ω. In fact, the remaining boundary condition must restrict $\boldsymbol{\psi}$ normal to Γ.

We are somewhat free to select what the remaining boundary condition will be. Both the Dirichlet-type boundary condition $\boldsymbol{\psi}\cdot\boldsymbol{n} = 0$ and the Neumann-type boundary condition $(\boldsymbol{\Theta}(\boldsymbol{x})\nabla\boldsymbol{\psi})\boldsymbol{n}\cdot\boldsymbol{n} = 0$ are possible candidates which would close the equations. Another option is to enforce a weighted average of those two boundary conditions. To be more specific, we may also consider the generalized (homogeneous) Robin boundary condition

$$\kappa\,\boldsymbol{\psi}\cdot\boldsymbol{n} + (\boldsymbol{\Theta}(\boldsymbol{x})\nabla\boldsymbol{\psi})\boldsymbol{n}\cdot\boldsymbol{n} = 0 \quad \text{on } \Gamma, \tag{13}$$

where the new model parameter $\kappa \geq 0$ could be inferred from available data. We choose to close the system with eq. (13) because it is flexible enough to fit a wide variety of data and simple to implement alongside eq. (12). We note that κ affects the horizontal velocity near the surface because of its control over the normal component of $\boldsymbol{\psi}$. Thus, in the proposed model, κ may be a parameter which distinguishes between different types of surfaces. We also note that, in the limit $\kappa \to \infty$, we recover the boundary condition

$\boldsymbol{\psi}\cdot\boldsymbol{n}=0$. Together with eq. (12), it implies the complete Dirichlet boundary condition, $\boldsymbol{\psi}=\mathbf{0}$ on Γ. Hereon, we use the notation $\kappa=\infty$ to indicate this special limiting scenario.

Thus, the boundary value problem given by eqs. (10), (12) and (13) eventually writes

$$\begin{cases} \big(I-\nabla\cdot(\boldsymbol{\Theta}(\boldsymbol{x})\nabla)\big)^{\alpha_1}\big(-\nabla\cdot(\boldsymbol{\Theta}(\boldsymbol{x})\nabla)\big)^{\alpha_2}\boldsymbol{\psi}=\mu\det(\boldsymbol{\Theta}(\boldsymbol{x}))^{\gamma/3}\boldsymbol{\eta} & \text{in } \Omega,\\ \boldsymbol{\psi}-(\boldsymbol{\psi}\cdot\boldsymbol{n})\boldsymbol{n}=0 & \text{on } \Gamma,\\ \kappa\,\boldsymbol{\psi}\cdot\boldsymbol{n}+(\boldsymbol{\Theta}(\boldsymbol{x})\nabla\boldsymbol{\psi})\boldsymbol{n}\cdot\boldsymbol{n}=0 & \text{on } \Gamma. \end{cases} \tag{14}$$

2.2.3 Fitting the Reynolds stress in the boundary layer

Let us consider the inhomogeneous turbulence model eq. (14), with fractional coefficients corresponding to the von Kármán energy spectrum eq. (4), on the open half space domain $\mathbb{R}^3_+=\{(x,y,z)\in\mathbb{R}^3\colon z>0\}$. Based on the supposed absence of shear, we also consider the following simple diagonal form for the diffusion tensor, in Cartesian coordinates:

$$\boldsymbol{\Theta}(z)=\begin{bmatrix} L_1(z)^2 & 0 & 0\\ 0 & L_2(z)^2 & 0\\ 0 & 0 & L_3(z)^2 \end{bmatrix}.$$

Defining $L(z)=\sqrt[3]{L_1(z)L_2(z)L_3(z)}$, the appropriate form of eq. (14) can be written as follows:

$$\begin{cases} \big(I-\nabla\cdot(\boldsymbol{\Theta}(z)\nabla)\big)^{17/12}\boldsymbol{\psi}=\mu\,L(z)^{17/6}\,\boldsymbol{\xi} & \text{in } \mathbb{R}^3_+,\\ \kappa\,\psi_3+L_3(z)^2\dfrac{\partial\psi_3}{\partial z}=\psi_1=\psi_2=0 & \text{at } z=0. \end{cases} \tag{15}$$

Both the Robin coefficient κ and an explicit parametric expression for each $L_i(z)$ give rise to a model design parameter vector, say $\boldsymbol{\theta}$. This vector $\boldsymbol{\theta}$ may then be subject to calibration with respect to experimental data.

Various statistical quantities of a turbulent flow field can be measured experimentally. Near a solid boundary, some of the most important of these quantities are the Reynolds stresses $\tau_{ij}=\langle u_iu_j\rangle$. In order to calibrate the parameters in eq. (15) to Reynolds stress data $\tau_{ij}^{\text{data}}(\boldsymbol{x}_l)$, collected at a number of locations in the flow domain $\boldsymbol{x}_l\in S$, we propose the following optimization problem:

$$\min_{\boldsymbol{\theta}}\ \mathcal{J}(\boldsymbol{\theta}),\quad \text{where}\quad \mathcal{J}(\boldsymbol{\theta})=\frac{1}{|S|}\sum_{\boldsymbol{x}_l\in S}\sum_{i,j=1}^{3}\Big(\tau_{ij}(\boldsymbol{x}_l;\boldsymbol{\theta})-\tau_{ij}^{\text{data}}(\boldsymbol{x}_l)\Big)^2. \tag{16}$$

Here, the design variable $\boldsymbol{\theta}$ denotes a coefficient vector taking accounting for all of the undetermined model parameters present in eq. (14). For instance, we use

$$\boldsymbol{\theta}=(c_{1,1},d_{1,1},c_{3,1},d_{3,1},\ldots,c_{1,K},d_{1,K},c_{3,K},d_{3,K},\kappa)\in\mathbb{R}^{4K+1},$$

where $c_{i,k}$ and $d_{i,k}$, $i=1,3$, $k=1,\ldots,K$, appear in the representation of each $L_i(z)$ with $K=2$ terms:

$$L_i(z)=L_\infty\cdot\left(1+\sum_{k=1}^{K}c_{i,k}\,\mathrm{e}^{-d_{i,k}\frac{z}{L_\infty}}\right), \tag{17}$$

with each $d_{i,k}\geq 0$, $c_{1,k}=c_{2,k}$ and $d_{1,k}=d_{2,k}$.

This process of model calibration is important because wall roughness, Reynolds number, and the nature of the turbulence may affect the near-wall statistics [52] and may be

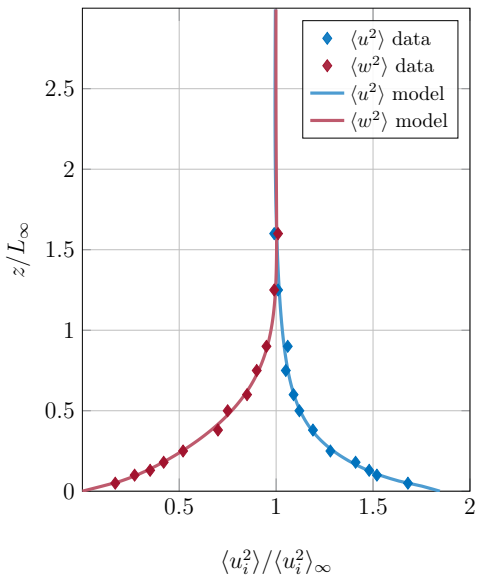

(a) Reynolds stress data from [58] compared with Reynolds stresses from the calibrated SFBL turbulence model (15). Observe that the model is able to closely fit the experimental data.

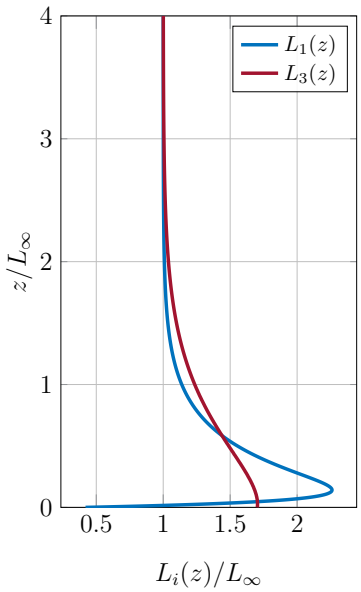

von Kármán model	
Parameter	Value
$c_{1,1}$	2.22
$c_{1,2}$	−2.80
$c_{3,1}$	5.04
$c_{3,2}$	−4.33
$d_{1,1}$	2.78
$d_{1,2}$	17.38
$d_{3,1}$	2.17
$d_{3,2}$	2.55
κ/L_∞	4.02

(b) Optimal diffusion coefficients $L_i(z)$ and Robin constant κ determined by fitting the Reynolds stress data in fig. 4a. Note that $L_1(z) = L_2(z)$.

Figure 4: Calibration of the SFBL turbulence model.

incorporated through proper parameter selection. Taking only two terms in each expansion above ($K = 2$), we arrive through calibration at a statistical model which closely matches the experimental data found in Thomas and Hancock [58]. Note that with such a model, $L_1(z) = L_2(z)$ and each $L_i(z)$ exponentially converges to the homogeneous length scale L_∞, as $z \to \infty$, as illustrated in fig. 4b. The exact definitions of the optimized model parameters used in the results above are stated explicitly in the table in fig. 4b. The difference between the Reynolds stress profiles in the calibrated model and the corresponding experimental data is depicted in fig. 4a. Because this model has many free parameters which can be calibrated to experimental data, it is much more flexible than the classical theory proposed by Hunt et al. [26, 27, 29].

2.3 A data-driven nonlocal turbulence model for the atmospheric boundary layer

It is typically not possible to directly measure a spectral tensor Φ_{ij} in a shearing flow. Instead, one often collects the one-point spectra[55]

$$F_{ij}(k_1) = \frac{1}{2\pi} \int_{-\infty}^{\infty} R_{ij}(r_1, 0, 0)\, \mathrm{e}^{-\mathrm{i}\, k_1 \cdot r_1}\, \mathrm{d}r_1,$$

with $i, j = 1, 2, 3$.

Obviously, the one-point spectra cannot give a complete description of the turbulent wind field. For this reason, it is necessary to construct physical models which can fit

these experimental observations. One of the issues in constructing these models is that turbulence in the atmospheric boundary layer is not spatially homogeneous. Nevertheless, the common surface layer scaling assumption [34] is that the length scales are proportional to z and the variances are proportional to u_*^2. For instance, after analyzing measurements taken above flat homogeneous terrain in Kansas, Kaimal et al.[34] proposed taking

$$\frac{k_1 F_{11}(k_1 z)}{u_*^2} = J_1(f) := \frac{52.5f}{(1+33f)^{5/3}}, \tag{18a}$$

$$\frac{k_1 F_{22}(k_1 z)}{u_*^2} = J_2(f) := \frac{8.5f}{(1+9.5f)^{5/3}}, \tag{18b}$$

$$\frac{k_1 F_{33}(k_1 z)}{u_*^2} = J_3(f) := \frac{1.05f}{1+5.3f^{5/3}}, \tag{18c}$$

where $f = (2\pi)^{-1} k_1 z$, alongside $F_{12} = F_{23} = 0$ and

$$-\frac{k_1 F_{13}(k_1 z)}{u_*^2} = J_4(f) := \frac{7f}{(1+9.6f)^{12/5}}. \tag{18d}$$

In section 2.3.3, we will use these equations as filtered measurement data for benchmarking the DRD model.

2.3.1 Rapid distortion

The rapid distortion equations [see, e.g., 28, 52, 59] are a linearization of the Navier–Stokes equations in free space which holds when the turbulence-to-mean-shear time scale ratio is arbitrarily large. To write them, we must first define the average total derivative of the turbulent fluctuations, namely

$$\frac{\bar{D}u_i}{\bar{D}t} = \frac{\partial u_i}{\partial t} + \langle U_j \rangle \frac{\partial u_i}{\partial x_j}.$$

With this definition in hand, the rapid distortion equations are

$$\frac{\bar{D}u_i}{\bar{D}t} = -u_i \frac{\partial \langle U_j \rangle}{\partial x_i} - \frac{1}{\rho}\frac{\partial p}{\partial x_i}, \tag{19a}$$

$$\frac{1}{\rho}\Delta p = -2\frac{\partial \langle U_i \rangle}{\partial x_j}\frac{\partial u_j}{\partial x_i}, \tag{19b}$$

where ρ and p stand for the mass density and the hydrostatic pressure, respectively.

With the uniform-shear mean profile $\langle \mathbf{U} \rangle = (A + Bz, 0, 0)$, the solution can be written in terms of an evolving wavevector $\boldsymbol{k}(t) = (k_1(t), k_2(t), k_3(t))$ and a non-dimensional time parameter $\tau = Bt$. For greater perspective, we begin with the general case where $\partial \langle U_i \rangle / \partial x_j$ is a constant tensor.

First, we define the rate of change of each frequency $\boldsymbol{k}(t)$ as follows:

$$\mathrm{d}k_i/\mathrm{d}t = -k_j \partial \langle U_j \rangle / \partial x_i. \tag{20}$$

We then have the following Fourier representation of the average total derivative of $\mathbf{u}$:

$$\begin{aligned}\frac{\bar{D}u_i}{\bar{D}t} &= \int_{\mathbb{R}^3} \mathrm{e}^{\mathrm{i}\,\boldsymbol{k}\cdot\boldsymbol{x}} \left(\left(\frac{\partial}{\partial t} + \frac{\mathrm{d}k_j}{\mathrm{d}t}\frac{\partial}{\partial k_j} \right) \mathrm{d}Z_i(\boldsymbol{k},t) \right) \\ &= \int_{\mathbb{R}^3} \mathrm{e}^{\mathrm{i}\,\boldsymbol{k}\cdot\boldsymbol{x}} \left(\frac{\bar{D}\,\mathrm{d}Z_i(\boldsymbol{k},t)}{\bar{D}t} \right).\end{aligned} \tag{21}$$

With these expressions, the Fourier representation of eq. (19) amounts to

$$\frac{\bar{D}\,\mathrm{d}Z_j(\boldsymbol{k},t)}{\bar{D}t} = \frac{\partial U_\ell}{\partial x_k}\left(2\frac{k_j k_\ell}{k^2} - \delta_{j\ell} \right) \mathrm{d}Z_k(\boldsymbol{k},t)\,, \tag{22}$$

which must be accompanied by the initial state $\mathrm{d}\boldsymbol{Z}(\boldsymbol{k}(0),0) = \mathrm{d}\boldsymbol{Z}_0(\boldsymbol{k}(0))$. From now on, we use the notation $\boldsymbol{k}_0 = \boldsymbol{k}(0) = (k_{10}, k_{20}, k_{30})$ to denote the initial wavevector.

In the uniform shear scenario $\langle \mathbf{U} \rangle = (A + Bz, 0, 0)$, the solution to eq. (22) may be written as follows:

$$\mathrm{d}\mathbf{Z}(\boldsymbol{k}(t),t) = \boldsymbol{D}_\tau(\boldsymbol{k})\,\mathrm{d}\mathbf{Z}(\boldsymbol{k}_0,0), \tag{23}$$

where

$$\boldsymbol{D}_\tau(\boldsymbol{k}) = \begin{bmatrix} 1 & 0 & \zeta_1 \\ 0 & 1 & \zeta_2 \\ 0 & 0 & \zeta_3 \end{bmatrix}, \qquad \boldsymbol{k} = \begin{bmatrix} 1 & 0 & 0 \\ 0 & 1 & 0 \\ -\tau & 0 & 1 \end{bmatrix} \boldsymbol{k}_0.$$

In the expression for $\boldsymbol{D}_\tau(\boldsymbol{k})$, the non-dimensional coefficients $\zeta_i = \zeta_i(\boldsymbol{k},\tau)$, $i = 1,2,3$, are defined

$$\zeta_1 = C_1 - C_2 k_2/k_1, \quad \zeta_2 = C_1 k_2/k_1 + C_2, \quad \zeta_3 = k_0^2/k^2,$$

where $k_0 = |\boldsymbol{k}_0|$ and

$$\begin{aligned} C_1 &= \frac{\tau k_1^2 (k_0^2 - 2k_{30}^2 + \tau k_1 k_{30})}{k^2(k_1^2 + k_2^2)}, \\ C_2 &= \frac{k_2 k_0^2}{(k_1^2+k_2^2)^{3/2}} \arctan x \Big|_{k_3/\sqrt{k_1^2+k_2^2}}^{k_{30}/\sqrt{k_1^2+k_2^2}}. \end{aligned}$$

All that is left is to set the initial state $\mathrm{d}\boldsymbol{Z}(\boldsymbol{k}_0,0) = \mathrm{d}\boldsymbol{Z}_0(\boldsymbol{k}_0)$. We define the initial state to be a Gaussian random field,

$$\mathrm{d}\boldsymbol{Z}_0(\boldsymbol{k}_0) = \boldsymbol{G}_0(\boldsymbol{k}_0)\,\mathrm{d}\boldsymbol{W}(\boldsymbol{k}_0), \tag{24}$$

with $\boldsymbol{G}_0(\boldsymbol{k}_0)$ induced by the isotropic spectral tensor (3) as follows,

$$\boldsymbol{G}_0(\boldsymbol{k}_0)\,\boldsymbol{G}_0^*(\boldsymbol{k}_0) = \Phi^{\mathrm{VK}}(\boldsymbol{k}_0).$$

We have now uniquely defined $\Phi(\boldsymbol{k},\tau)$. First, following from section 2.1 and eqs. (23) and (24), we may write $\hat{\mathbf{u}}(\boldsymbol{k}) = \mathsf{D}_\tau(\boldsymbol{k})\,\boldsymbol{G}_0(\boldsymbol{k}_0)\,\hat{\boldsymbol{\xi}}(\boldsymbol{k}_0)$. Second, by eq. (2) and the identity $\langle \bar{\hat{\xi}}_i \hat{\xi}_j \rangle = \delta_{ij}$, we have that

$$\begin{aligned}\Phi(\boldsymbol{k},\tau) &= \langle \hat{\mathbf{u}}(\boldsymbol{k}) \hat{\mathbf{u}}^*(\boldsymbol{k}) \rangle \\ &= \mathsf{D}_\tau(\boldsymbol{k})\,\boldsymbol{G}_0(\boldsymbol{k}_0) \langle \hat{\boldsymbol{\xi}}(\boldsymbol{k}_0)\ \hat{\boldsymbol{\xi}}^*(\boldsymbol{k}_0) \rangle\, \boldsymbol{G}_0^*(\boldsymbol{k}_0)\,\mathsf{D}_\tau^*(\boldsymbol{k}) \\ &= \mathsf{D}_\tau(\boldsymbol{k})\,\boldsymbol{G}_0(\boldsymbol{k}_0)\,\boldsymbol{G}_0^*(\boldsymbol{k}_0)\,\mathsf{D}_\tau^*(\boldsymbol{k}) \\ &= \mathsf{D}_\tau(\boldsymbol{k})\,\Phi^{\mathrm{VK}}(\boldsymbol{k}_0)\,\mathsf{D}_\tau^*(\boldsymbol{k}).\end{aligned}$$

2.3.2 Neural network model for the eddy lifetime

The spectral tensor $\Phi(\boldsymbol{k}, \tau)$ characterizes a time-dependent family of anisotropic covariance kernels which are stretched in the direction of the constant mean shear. One flaw in this model is that physical eddies will break apart after a certain amount of distortion.

An important extension of the rapid distortion model involves replacing the distortion parameter τ by a wavenumber-dependent *eddy lifetime* function $\tau(\boldsymbol{k})$. The benefit of this substitution is two-fold: not only does it produce a stationary (time-*independent*) spectral tensor $\Phi(\boldsymbol{k}, \tau(\boldsymbol{k}))$, but it provides a mechanism to recover missing physics which are neglected in the original modeling assumptions.

Various eddy lifetime models have been proposed in the literature [17, 43, 47], each of which involves restricting the eddy lifetime τ to a radial function of the wavevector, $\tau = \tau(k)$. For instance, a widely used radial function is presented in [47] and results in a spectral tensor model which was subsequently standardized by the IEC [30]. In this approach, the destruction of an eddy with size k^{-1} is assumed to be mainly due to eddies of comparable or smaller size. Thus, the square of the characteristic velocity of all influential eddies is given by $\int_k^\infty E(p)\,\mathrm{d}p$. By matching units, the eddy lifetime τ may be proportional to a length scale divided by a velocity , e.g.,

$$\tau \propto k^{-1} \left[\int_k^\infty E(p)\,\mathrm{d}p \right]^{-\frac{1}{2}}. \tag{25}$$

After substituting eq. (4), this expression results in

$$\tau^{\mathrm{IEC}}(k) = \frac{T B^{-1} (kL)^{-\frac{2}{3}}}{\sqrt{{}_2F_1(1/3, 17/6; 4/3; -(kL)^{-2})}}, \tag{26}$$

where ${}_2F_1(a, b; c; x)$ denotes the hypergeometric function, and the time scale T is a free parameter. To facilitate an accurate comparison to this model in Section 2.3.3, we point out that

$$\tau^{\mathrm{IEC}}(k) \propto \begin{cases} k^{-1} & \text{for } k \to 0, \\ k^{-3/2} & \text{for } k \to \infty. \end{cases}$$

Substituting eq. (26) into the rapid distortion spectral tensor, results in the Mann uniform shear model,

$$\Phi^{\mathrm{IEC}}(\boldsymbol{k}) = \Phi(\boldsymbol{k}, \tau^{\mathrm{IEC}}(|\boldsymbol{k}|)). \tag{27}$$

Expanded formulas for $\Phi^{\mathrm{IEC}}(\boldsymbol{k})$ can be found in [30, 47].

Given the anisotropic nature of shear flow, it is natural to expect that the lifetime of an eddy could depend on its initial spatial orientation. However, it is also clear that this dependence should satisfy some basic physical conditions. For instance, owing to translational symmetry of the flow in the transversal direction (y-axis), we expect $\tau(\boldsymbol{k})$ to be an even function of k_2. We note that this restriction guarantees that the transversal components of the one-point cospectra, F_{12} and F_{23}, vanish; cf. eq. (18).

We now propose a method to discover complete wavevector eddy lifetime functions $\tau(\boldsymbol{k})$ from measured data. Our approach involves writing $\tau(\boldsymbol{k})$ as a feedforward neural network with the wavevector $\boldsymbol{k}$ as input. Then, learning its parameters by fitting the one-point spectra data, we identify the function $\tau(\boldsymbol{k})$ as well as the complete spectral tensor model.

Aside from physical symmetries, the eddy lifetime must satisfy certain asymptotic behavior in the limits $k \to 0$ and $k \to \infty$. To this end, we first rewrite the eddy lifetime function as follows:

$$\tau(\boldsymbol{k}) = \frac{T\,|\boldsymbol{a}|^{\nu-\frac{2}{3}}}{(1+|\boldsymbol{a}|^2)^{\nu/2}}, \qquad \boldsymbol{a} = \boldsymbol{a}(\boldsymbol{k}), \tag{28}$$

where T is characteristic timescale, ν is a tunable exponent, and $\boldsymbol{a}$ is a intermediary variable, which we refer to as the "augmented" wavevector. We will define $\boldsymbol{a}(\boldsymbol{k})$ in terms of a neural network $\boldsymbol{a} = \mathcal{O}(k)$ in both limits $k \to 0$ and $k \to \infty$. Therefore, the form of the fractional exponents in (28) will allow us to control the asymptotic behavior of $\tau(\boldsymbol{k})$. This is important since the asymptotic slopes are objects of discussion in the literature. Thus, while the slope at zero is controlled by ν, the well-known slope at infinity,[41, 47, 52] $k^{-2/3}$, is recovered for any value of ν.

We define

$$\boldsymbol{a}(\boldsymbol{k}) := \mathrm{abs}(\boldsymbol{k}) + \mathrm{NN}(\mathrm{abs}(\boldsymbol{k})). \tag{29}$$

Here, $\mathrm{abs}(\cdot)$ denotes the element-wise absolute value and $\mathrm{NN}(\cdot)$ is a fully-connected multilayer perceptron, namely

$$\mathrm{NN}(\boldsymbol{y}) := W_n\,\mathrm{ReLU} \circ \cdots \circ \mathrm{ReLU} \circ W_1 \boldsymbol{y}, \tag{30}$$

where $\mathrm{ReLU}(\cdot)$ stands for the rectified linear activation function and W_j, $j = 1, \ldots, n$, are dense matrices (no bias terms). The choice of a ReLU function is motivated by the requirement that $\mathrm{NN}(\boldsymbol{0}) = \boldsymbol{0}$, thus, $\boldsymbol{a}(\boldsymbol{0}) = \boldsymbol{0}$. Other activation functions, such as the softplus activation function will not guarantee this property.

Note that taking the absolute value of the first argument in eq. (29) provides a reflection symmetry in $\tau(\boldsymbol{k})$ with respect to each Cartesian axis. This is obviously more than necessary to satisfy symmetry in the k_2-component. Our experience has shown that that there is no benefit to the accuracy of the model, when fitting one-point spectra data, if we relax the symmetry the k_1- and k_3-components.

We use one input and one output layer, each of size 3, accompanied by $n-2$ hidden layers of size m. In other words, $W_1 \in \mathbb{R}^{3\times m}$, $W_j \in \mathbb{R}^{m\times m}$, $j = 2, \ldots, n-1$, and $W_n \in \mathbb{R}^{m\times 3}$, whose sum total of entries constitute a new vector of learnable parameters $\boldsymbol{\theta}_{\mathrm{NN}}$. Note that if any $W_j = 0$, $j = 1, \ldots n$, then $\mathrm{NN} = 0$. This forces the magnitude of the augmented wavevector to agree with the true wavenumber, $|\boldsymbol{a}| = k$. From this point-of-view the neural network acts in a way like a piecewise-linear perturbation of the original wavevector.

Once the eddy lifetime function eq. (28) has been substituted into the rapid distortion model $\Phi(\boldsymbol{k}, \tau)$, we arrive at the DRD spectral tensor model:

$$\Phi^{\mathrm{DRD}}(\boldsymbol{k}, \boldsymbol{\theta}) := \Phi(\boldsymbol{k}, \tau(\boldsymbol{k})), \tag{31}$$

where the vector of all learnable parameters, i.e.,

$$\boldsymbol{\theta} = \{C, L, T, \nu, \boldsymbol{\theta}_{\mathrm{NN}}\}, \tag{32}$$

consists of the spectrum amplitude $C := c_0^2\,\varepsilon^{2/3}/u_*^2$, the characteristic length and time sales, L and T, respectively, the exponent ν and the weights $\boldsymbol{\theta}_{\mathrm{NN}}$ of the neural network (30).

2.3.3 Fitting the one-point spectra

In this section, we discuss various aspects of the model regression problem which calibrates the eddy lifetime $\tau(\boldsymbol{k})$ together with the other free parameters in the DRD model eq. (32). More specifically, we document the problem formulation, state important details from our implementation,[36] and summarize our results.

Let us consider the one-point spectra eq. (18) on the interval $\mathcal{D} = [0.1, 100]$. We wish to find the model parameters $\boldsymbol{\theta}$ which best fit this data. To set the stage, define

$$\tilde{F}_{ij}(k_1; \boldsymbol{\theta}) = \int_{-\infty}^{\infty} \int_{-\infty}^{\infty} \Phi_{ij}^{\mathrm{DRD}}(\boldsymbol{k}, \boldsymbol{\theta}) \, \mathrm{d}k_2 \, \mathrm{d}k_3, \tag{33}$$

and

$$\tilde{J}_i(f; \boldsymbol{\theta}) = C \, k_1 \tilde{F}_{ii}(k_1 z; \boldsymbol{\theta}), \quad i = 1, 2, 3, \tag{34}$$

and $\tilde{J}_4(f; \boldsymbol{\theta}) = C \, k_1 \tilde{F}_{13}(k_1 z; \boldsymbol{\theta})$, where $f = (2\pi)^{-1} k_1 z$. Note that the learnable magnitude C involves the constants $c_0^2 \, \varepsilon^{2/3}$ and u_*^2.

To find the optimal parameter vector $\boldsymbol{\theta}_{\mathrm{opt}}$, we solve the optimization problem

$$\min_{\boldsymbol{\theta}} \big\{ \mathrm{MSE}[\boldsymbol{\theta}] + \alpha \, \mathrm{Pen}[\boldsymbol{\theta}] + \beta \, \mathrm{Reg}[\boldsymbol{\theta}_{\mathrm{NN}}] \big\}, \tag{35}$$

where $\alpha, \beta \geq 0$ and each function $\mathrm{MSE}[\boldsymbol{\theta}]$, $\mathrm{Pen}[\boldsymbol{\theta}]$, and $\mathrm{Reg}[\boldsymbol{\theta}_{\mathrm{NN}}]$ is defined as follows. The mean squared error is defined as

$$\mathrm{MSE}[\boldsymbol{\theta}] := \frac{1}{L} \sum_{i=1}^{4} \sum_{j=1}^{L} \big(\log |J_i(f_j)| - \log |\tilde{J}_i(f_j, \boldsymbol{\theta})| \big)^2, \tag{36}$$

where L is the number of the data points $f_j \in \mathcal{D}$. The data $J_i(f_j)$ is evaluated using the Kaimal spectra (18a)–(18d). The penalization term is defined as

$$\mathrm{Pen}[\boldsymbol{\theta}] := \frac{1}{|\mathcal{D}|} \sum_{i=1}^{4} \left\| \mathrm{ReLU}\left(\frac{\partial^2 \log \left| \tilde{J}_i(\cdot, \boldsymbol{\theta}) \right|}{(\partial \, \log k_1)^2} \right) \right\|_{\mathcal{D}}^2, \tag{37}$$

where $|\mathcal{D}| = \|1\|_{\mathcal{D}}$ and the norm $\|\cdot\|_{\mathcal{D}}$ is defined

$$\|g\|_{\mathcal{D}}^2 := \int_{\mathcal{D}} |g(f)|^2 \, \mathrm{d}(\log f). \tag{38}$$

This term penalizes the curvature of the log-spectra in order to obtain convex curves and to minimize oscillations, thus protecting against overfitting. Associating $\boldsymbol{\theta}_{\mathrm{NN}}$ with a vector $(\theta_1, \ldots, \theta_N) \in \mathbb{R}^N$, we write

$$\mathrm{Reg}[\boldsymbol{\theta}_{\mathrm{NN}}] := \frac{1}{N} \sum_{i=1}^{N} \theta_{\mathrm{NN},i}^2, \tag{39}$$

where N denotes the total number of weights of the neural network eq. (30). The term accelerates convergence and also helps to avoid overfitting.

The model regression problem eq. (35) is implemented and solved using the PyTorch package [50]. In particular, we use a full-batch L-BFGS optimization algorithm with the strong Wolfe line search method and learning rate equal to 1. We use $n = 2$ hidden layers of size $m = 10$ and begin by using the penalty and regularization parameters $\alpha = 1$ and $\beta = 10^{-5}$, respectively.

The integrals in (33) are truncated and approximated using the trapezoidal quadrature rule on a logarithmic grid from 10^{-3} to 10^{3} with 100×100 nodes spanning the frequencies k_2 and k_3. The second derivative in (37) is approximated with central finite differences. And the norm eq. (38) is approximated using the trapezoidal rule.

The IEC-recommended spectral tensor model eq. (27) is calibrated in [48] to fit the Kaimal spectra. [33, 34] In our notation, its three free parameters are L, T, and C. We use the fitted values from [48], i.e., $L = 0.59$, $T = 3.9$, $C = 3.2$, to compare against the DRD model.

In our first experiment, we *fix* the exponent $\nu = -\frac{1}{3}$. This is done so that $\tau(\boldsymbol{k})$ matches the slope of τ^{IEC} as $k \to 0$; in other words, so that

$$\tau(\boldsymbol{k}) \propto \tau^{\mathrm{IEC}}(k) \propto k^{-1} \quad \text{for } k \to 0.$$

We then set the initial scales of the DRD model to, $L = 0.59$, $T = 3.9$, $C = 3.2$ and initialize the weights $\boldsymbol{\theta}_{\mathrm{NN}}$ with random values drawn from additive Gaussian white noise with variance 1×10^{-2}. We consider the range $\mathcal{D} = [0.1, 100]$ and sample the data points $f_j \in \mathcal{D}$ using a logarithmic grid of $N_{nodes} = 20$ nodes. The result of fitting the Kaimal spectra can be seen in Figure 5b. This can be compared to the best fit produced by eq. (27), depicted in Figure 5a. We observe that the DRD model presents a much better fit than the Mann uniform shear model, by a clear order of magnitude. In Figure 6, we plot the convergence of the mean squared error (36) throughout the optimization procedure.

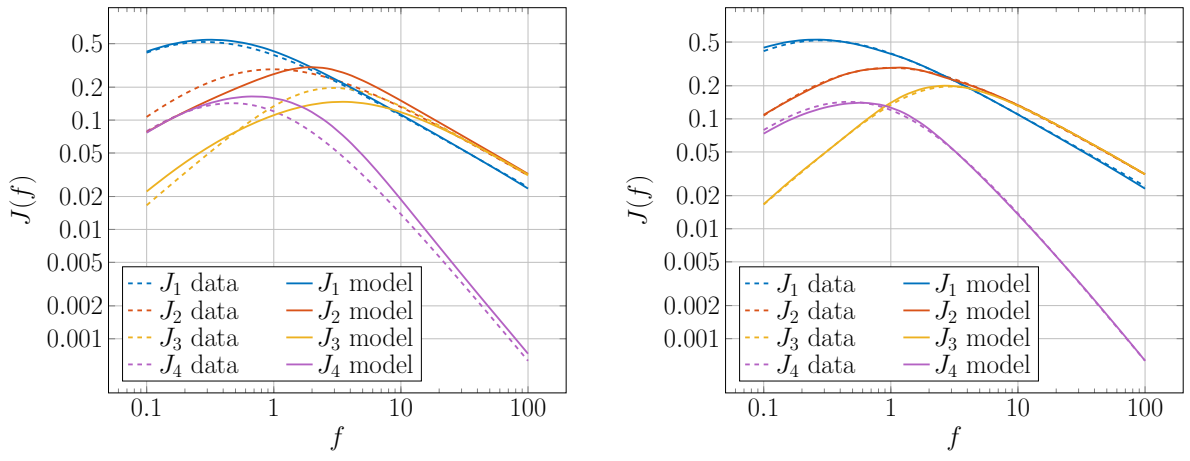

(a) IEC 61400-1 model.

(b) DRD model with $\nu = -\frac{1}{3}$ (fixed).

Figure 5: Comparison of the spectral models fitting the Kaimal spectra.

In our second experiment, we proceed by fitting a perturbation of the Kaimal spectra with multiplicative log-normal noise. Note that in this case, the use of the penalty term (37) is important to avoid overfitting the noisy data. On the other hand, the regularization term must be tuned to avoid local minima of the loss function eq. (35). For

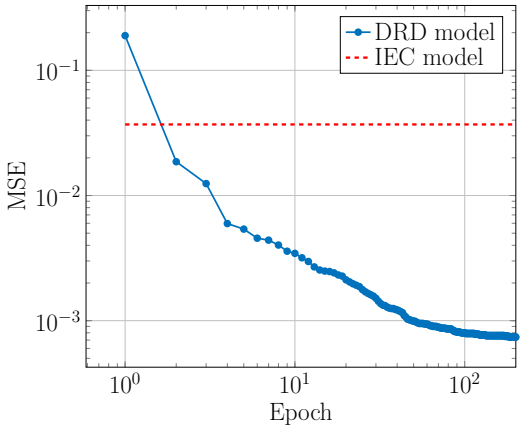

Figure 6: Convergence of the mean squared error (36) during training to fit the one-point spectra in Figure 5b. The accuracy is more than an order of magnitude better than the IEC 61400-1 model, which achieves the fit shown in Figure 5a.

best results, we increase the regularization parameter to $\beta = 10^{-2}$. All other parameters are left unchanged.

In this example, we illustrate the possibility of learning the slope of the eddy lifetime function in the energy-containing subrange. More specifically, we now suppose that the exponent ν is a learnable parameter, and we aim to calibrate it in addition to the remaining model parameters. To this end, we consider the extended range $\mathcal{D} = [0.01, 100]$, discretized with a logarithmic grid of $N_{nodes} = 40$ nodes. It is necessary to extended the range of the the data into low wavenumbers, in order to get an accurate estimate of ν. Our results are shown in Figure 7. Here, we see a good fit to the data. The calibrated slope is given by $\nu = -0.55$.

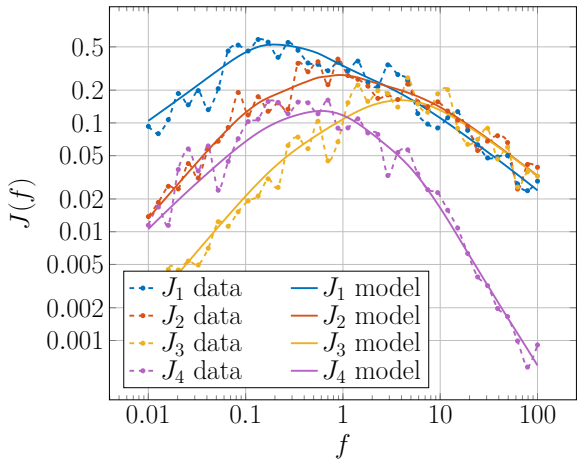

Figure 7: Fitting a noisy Kaimal spectra with the DRD model.

3 Stochastic optimization of twisted tapered tower

3.1 Introduction and motivation

Wind-induced lateral loads are a significant design consideration for super tall buildings. Designing these super tall buildings only based on design codes [1, 4] is not recommended, and detailed investigations are required for tall buildings. This aspect is of particular interest when the geometry of the building is nonstandard in nature. Over the past few decades CWE has matured such as to predict the pressure field and other wind behavior around a structure accurately [3, 11, 51].

Many mitigation strategies are developed and widely used in practice to reduce the wind action on the structure. Modification in geometric parameters of the building shape is effective in reducing the wind loads on tall buildings. These local or global geometric modifications can significantly reduce the total force and moments in the tall building. Providing openings in the building [20], corner modifications [14], twisting [21], tapering and stepping [31] are used in practice.The various mitigation strategies are summarized in [5]. CWE tools provide an environment to combine it with existing optimization strategies. Elshaer [21] presented one such optimization framework for determining the optimal shape of tall buildings under wind loads using CWE. A Neural network-based genetic algorithm is used for the optimization. However, the optimization considered was deterministic. A framework for optimization of building geometries considering the uncertainties of the incoming wind and terrain conditions is presented here. The global geometric parameters are optimized to reduce the total reaction of the building towards incoming uncertain wind flow. Considering the uncertainties in the wind inlet, various stochastic optimization strategies may be employed. Optimization of the mean, optimization based on the robust mean and standard deviation [22] or reliability-based optimization [25] may be employed. Rockafellar et al. [54] proposed the risk-averse optimization by conditional value at risk [53]. A risk-averse optimization is also employed in the current study, and the results are presented in this report.

The geometry of the building is motivated by the absolute world tower. This report is complementary to Deliverable 6.5 [7] and Deliverable 6.4 [6] . These reports may be referred to for a more theoretical formulation of the optimization problem and the method in detail.

3.2 Modelling of the wind flow around the building

Figure 8 shows the adopted CFD domain and boundary conditions. The global geometric modifications are taken into account in the current optimization study. The building has an elliptical cross-section with an sdome at the top. Two global geometric parameters affect the building geometry. Two global geometric modifications are considered as the tapering and twisting of the geometry along with the height. The design parameters considered are hence the minor diameter at the top and the twisting of the top cross-section with respect to the base to the building.

Table 1 tabulated the fluid properties and the dimensions of the building for the initial design configuration. The initial top cross-section is circular with a diameter of 30m. The Reynolds number for the problem is computed, and it shows that the problem at hand is highly turbulent. The incompressible Navier-Stokes equation is used to model the wind flow around the building as in Equation (40)

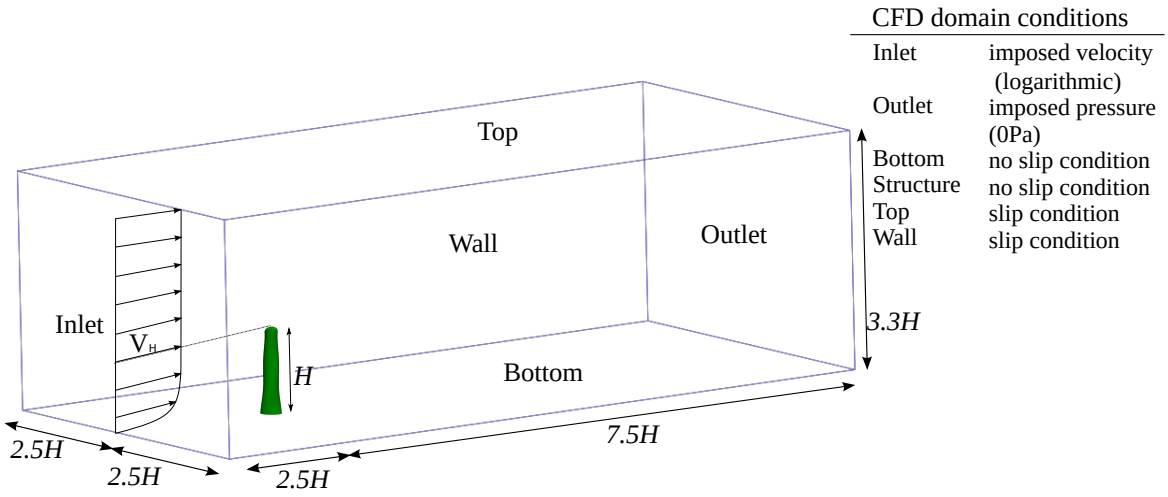

Figure 8: Details of the fluid simulation, domain and boundary conditions

Table 1: Fluid properties and building details

Quantity	Value	Unit
Density	1.225	kg/m^3
Viscosity	1.507E-5	m^2/s
Dynamic viscosity	1.846E-5	Ns/m^2
Reynolds number	9.7E7	
Characteristic length	45	m
Height of the building	180	m
Major base diameter	45	m
Minor base diameter	30	m
Major diameter at top (initial)	30	m
Minor diameter at top (initial)	30	m
Angle of twist (initial)	65	$^\circ$

$$\begin{aligned} \frac{\partial \mathbf{u}}{\partial t} + \mathbf{u}\cdot\nabla\mathbf{u} - \nu\Delta\mathbf{u} + \nabla p = \mathbf{f} \quad &\text{on } \Omega\,,\ t\in[0,T] \\ \nabla\cdot\mathbf{u} = 0 \quad &\text{on } \Omega\,,\ t\in[0,T]\,, \end{aligned} \tag{40}$$

where $\mathbf{u}$ is the velocity, p is the pressure, ν is the kinematic viscosity, $\mathbf{f}$ is the body forces, Ω is the domain and $[0,T]$ is the time window.

The wind flow around the building is simulated in Kratos Multiphysics solver .A vms formulation from [18] is adopted for the flow solver. The fluid domain is modeled with *fractional step elements*.

Within this work, the geometry subject to shape optimization encounters shape updates at each of the optimization steps. This renders the deployment of mesh moving CFD approaches not optimal since the geometry updates might be large enough to distort the fluid elements to such an extent that the results are meaningless. Therefore a remeshing approach is adopted for the current study to generate the bodyfitted meshes automatically. MMG remesher is used for the remeshing of the fluid domain.

The geometry is meshed with different refinement zones and the details of the adopted initial mesh is shown in figure 9. This initial mesh is used for all the optimization steps and UQ samples.

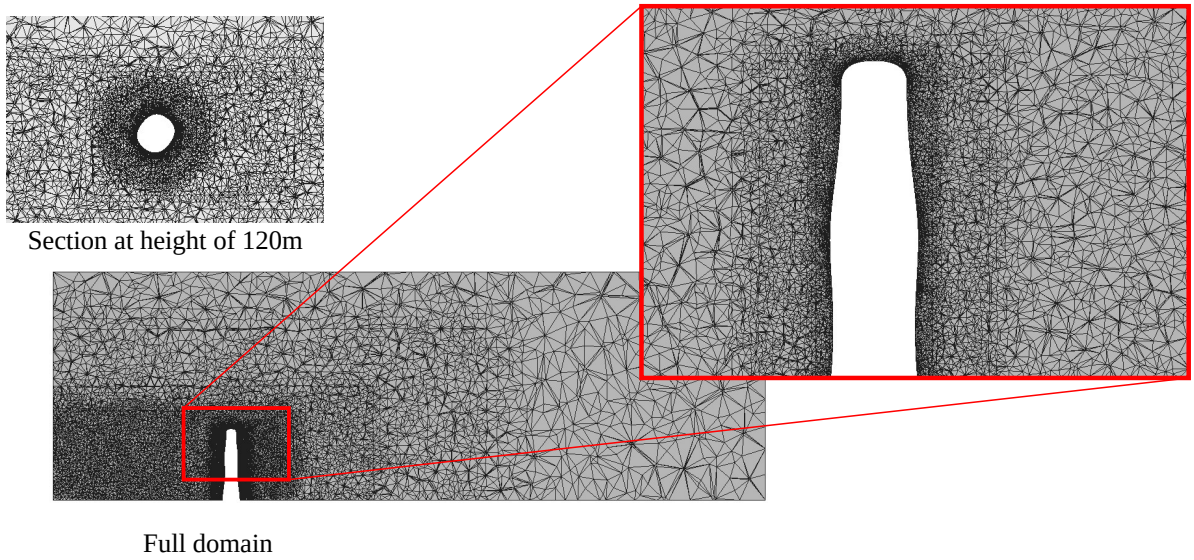

Figure 9: Details of the adopted mesh for the simulation

3.3 Quantities of Interest

The quantities of interest considered in the current study are the forces and base moments as elaborated in Deliverable 6.4[6] . The quantities of interest are the total reaction force $F_X(t), F_Y(t), F_Z(t)$ in all the three directions and the moment of the forces at the base. These quantities are of particular interest for the design of the foundation and the structural system of the building. By reducing these global values a reduction in total cost of the building can be achieved. These quantities of interest are minimized with the angle of twist and tapering as design parameters.

3.4 Uncertainties in the incoming wind

Here, a physical model for uncertainty quantification in wind engineering is elaborated. As is typical in the wind engineering community, we model the natural wind effects in the atmospheric boundary layer by decomposing the incoming velocity field, $\boldsymbol{u} = \overline{\boldsymbol{u}} + \boldsymbol{u}'$, into its stationary *mean profile* $\overline{\boldsymbol{u}}$ and its unsteady *turbulent fluctuations* $\boldsymbol{u}'$. Under the assumptions of neutral stability, homogeneous roughness, the mean velocity $\overline{\boldsymbol{u}} = \overline{\boldsymbol{u}}(z)$ can be modeled by the following logarithmic profile [35]:

$$\overline{\boldsymbol{u}} = \frac{u_*}{\kappa} \ln\left(\frac{z}{z_0} + 1\right) \boldsymbol{e}(\theta)\,, \tag{41}$$

where $\kappa \approx 0.41$ is the von Karmán constant.

Each of the parameters u_*, θ, and z_0 in eq. (41) are random variables. It is often assumed that the friction velocity, averaged over all angles θ, obeys a Weibull distribution, Wieb(λ, k), with *scale* λ and *shape* k [35]. Likewise, statistic models for the wind angle θ

are often constructed using a mixture of von Mises distributions [15, 23]. Models for the friction velocity are not so well-studied. In this work, we assume that $z_0 \sim \text{Unif}(z_L, z_U)$, where z_L and z_U are positive constants inferred from the engineering codebook [32].

If u_*, θ, and z_0 are not independent random variables, because of nearby geographic features or persistent weather patterns. For example, consider the wind rose on the left-hand side of Figure 10, which indicates a strong dependence between u_* and θ in field measurements in Basel, Switzerland. In this work, we take care to use an empirical multivariate joint distribution to describe the dependence between these two variables. Relationships between z_0 and θ have been studied [35], but field data is less widely available to use in practice. Therefore, we take on the modeling assumption that z_0 is independent of both u_* and θ.

3.5 Wind rose models

In this work, we use an empirical copula-based model to replicate the dependence between the random variables u_* and θ. In particular, we use a dataset of mean wind velocities and directions collected at 10m above ground in Basel, Switzerland, from 2010-01-01 to 2015-12-31,[1] to construct our model; cf. Figure 10. Note that $u_* = \kappa \|\overline{\boldsymbol{u}}(z)\| / \ln(z/z_0 + 1)$, therefore, a copula model based on θ and the mean wind speed at a specified height z, namely $\|\overline{\boldsymbol{u}}(z)\|$, can also be used to characterize the relation the bivariate distribution of θ and u_*.

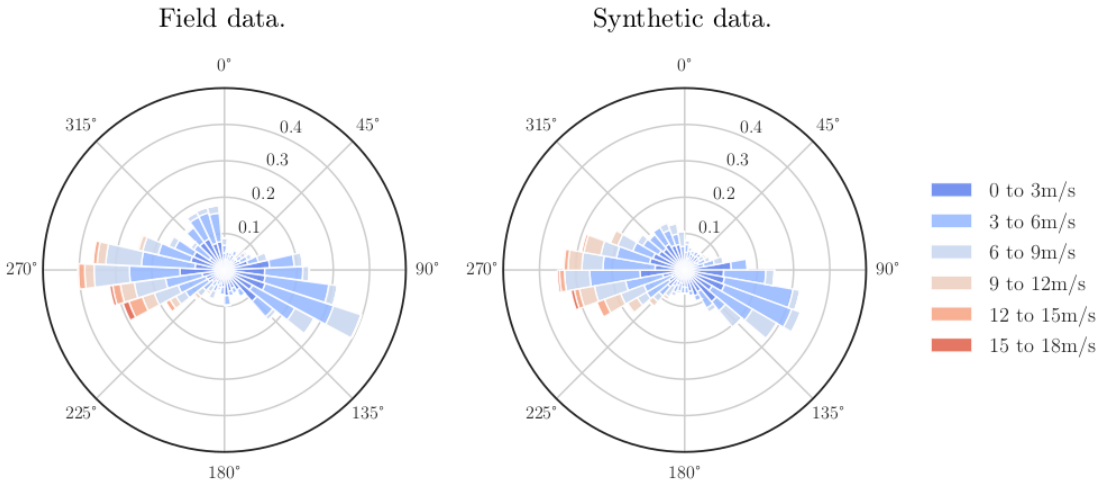

Figure 10: Wind Rose

Modeling turbulent fluctuations with physical wind gust statistics is significantly more challenging than modeling the mean profile. In this study, we choose to model the velocity fluctuations using the atmospheric boundary layer turbulence model proposed in [47, 48] and elaborated in detail in Deliverable 7.3 [10] . It is a widely used model for synthetic wind generation in the atmospheric boundary layer; see, e.g., [2, 30, 49]

[1] Available for free at `https://www.meteoblue.com`.

3.6 Optimization problem

For notational simplicity, Let $F(x)$ denote the mean optimization problem. At each design iterate x_k, we choose to approximate $F(x)$ with a sample average approximation; this is one of the more common procedures used in stochastic optimization [39].

Fix $T > 0$ and let $F^{(i)}(x) = \langle f(x; \omega^{(i)}, \boldsymbol{\xi}^{(i)}) \rangle_T$. For each design x_k in the optimization loop, denote

$$F_{S_k}(x_k) = \frac{1}{|S_k|} \sum_{i \in S_k} F^{(i)}(x_k)\,, \tag{42}$$

where each sample $(\omega^{(i)}, \boldsymbol{\xi}^{(i)})$ in the sample set S_k satisfies $\bar{u}^{(i)} > \mathrm{VaR}_{0.95}(\bar{u})$. In order to ensure that the samples in S_k follow the correct conditional distribution, we draw each $\boldsymbol{\xi}^{(i)}$ independently, but only populate S_k with the samples satisfying the constraint $\bar{u} > \mathrm{VaR}_{0.95}(\bar{u})$.

The gradient of each accepted sample, $\nabla F^{(i)}(x_k)$, can be computed via finite differences in the design variable $x \in \mathbb{R}^d$. In particular, for each sample $i \in S_k$, this involves $d+1$ numerical tunnel simulations. Due to the chaotic nature of the flow, an accurate gradient for an individual sample requires a long time interval [42], the exact length of which is problem-dependent. In addition, special care must be taken to select an appropriate finite difference increment in each component of design space.

Once each of the individual gradients $\nabla F^{(i)}(x_k)$ have been estimated, the sample average gradient,

$$\nabla F_{S_k}(x_k) = \frac{1}{|S_k|} \sum_{i \in S_k} \nabla F^{(i)}(x_k)\,, \tag{43}$$

may be formed as an approximation of the true gradient of $F(x_k)$. The first-order method we rely on in our work to arrive at the next iterate x_{k+1} is simply the traditional gradient descent strategy

$$x_{k+1} = x_k - \alpha_k \nabla F_{S_k}(x_k), \qquad \alpha_k > 0\,. \tag{44}$$

Our approach to the selection of the sample space size $|S_k|$, at each iterate, is determined adaptively base on an a posteriori estimate of the statistical error. In particular, the size of the sample space to grow as the optimal solution is converged upon. This strategy, which is outlined in the next subsection, has been shown to significantly reduce the cost in stochastic gradient descent [12, 13, 16]. The adaptive sampling is explained in details in deliverable 6.5[7] .

The expensive computation are run on Karolina super computer of the IT4Innovations cluster located in Ostrava, Czech Republic. PyCOMPSs [9, 46, 57] is the framework used for parallel computing.

3.7 OUU workflow

Within this work, the geometry subject to shape optimization encounters shape updates driven by the gradient-descent optimization algorithm employed. The adopted stochastic optimization workflow is detailed in this section. The optimization tries to minimize the observable of the selected QoI by looking for the best design parameters while considering the uncertainty from the incoming wind. The design parameters might also have some constraints from the architects and designers.

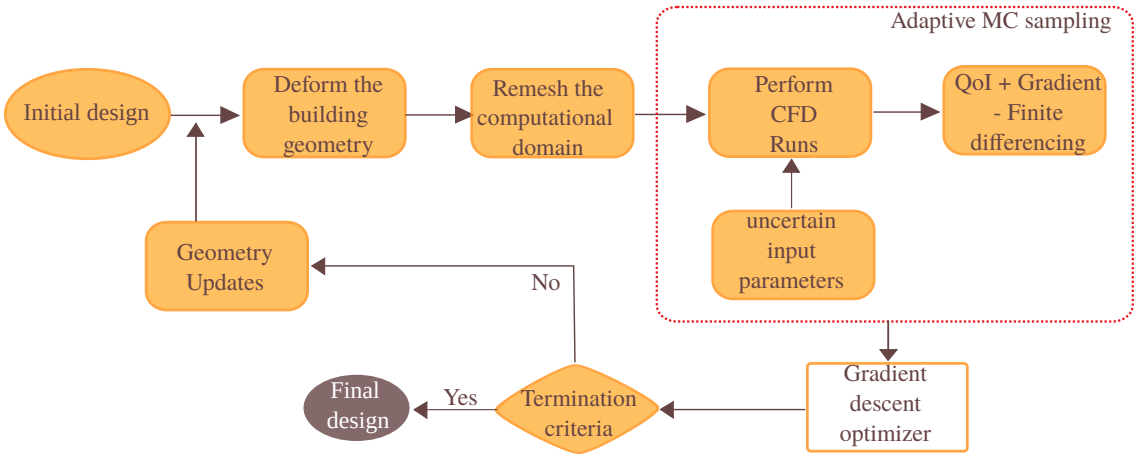

Figure 11: Details of the OUU workflow adopted

The OUU workflow begins by defining the objective function, design parameters, and uncertain input parameters. The objective function is the stochastic quantities of the QoI like the mean, mean + sd, CVAR, etc. The objective function value depends on the geometry of the building, which depends on the design parameters. The building geometry is parameterized to have the design parameters as the inputs. The background CFD mesh is remeshed to capture the new geometry and create the new body-fitted mesh.

In cases where the angle of arrival of the wind is also an uncertain input parameter, each uncertainty quantification samples require remeshing of the domain. The objective function is obtained by running the CFD simulations. The 3D CFD simulations are expensive, and an adaptive sampling strategy is adopted in the stochastic optimization workflow.

A finite-difference approach is used to compute the sensitivities. Since the number of design parameters is lower, the additional computations required for the sensitivities are not massive. Multiple evaluations of the CFD is required for each optimization step. It is realized by parallel evaluation of the samples. The QoI and Gradients are fed into the stochastic gradient descent optimizer. A gradient descent algorithm with fixed step sizes is adopted in the workflow. The optimization algorithm requires multiple iterations until it converges to the final design. The details of the optimization workflow are summarized in Figure 11.

3.8 Results

The optimization workflow is used for the stochastic optimization of the twisted tapered building until the optimization converges. Two stochastic optimization problems are carried out, One with the mean of the base moment as objective function and the other as the CVaR 90 of the base moment as objective function. Both problems were started from the same initial design. The initial design is a circular cross-section of 30m at the top with angle of twist of 65 degrees. Both the problem converges at 25 and 26 iterations, respectively. The initial and the final design of the building can be seen in Figure 12. It can be observed that the mean and CVaR optimization problem has converged two local

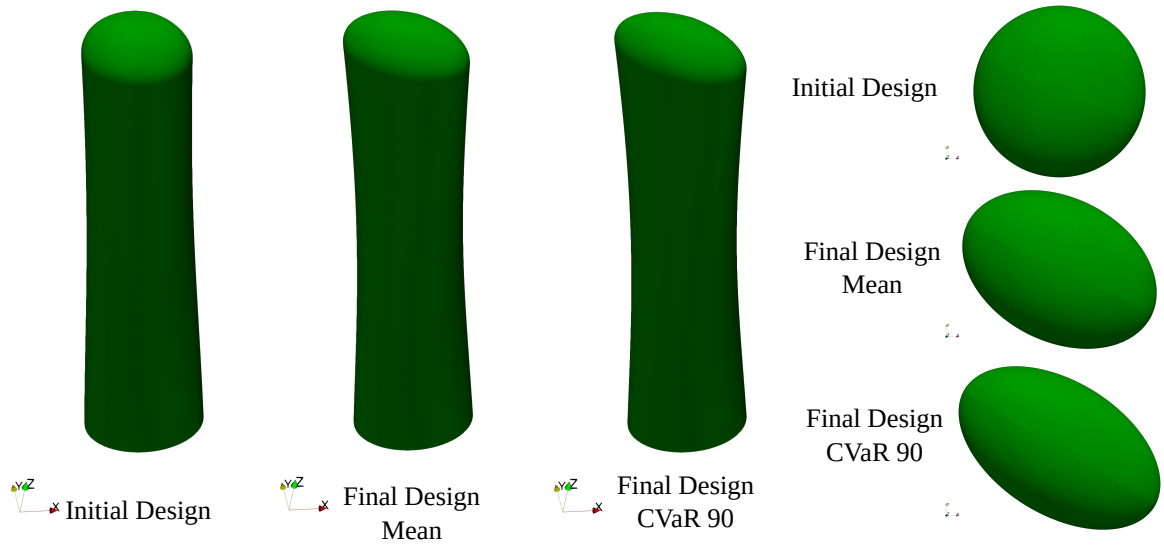

Figure 12: Shapes of the optimization results

minima, showing a difference in the final geometry. Figure13a and Figure 13b show the progress of the optimization at each steps. The top cross-section is shown.

The risk-neutral candidate design is shown in 14. The improvement in the objective function is illustrated in the figure. It can be seen that the objective function improves by 7% for the mean optimization problem. The plot also showcases the number of samples required for each of the optimization steps. The performance of the adaptive sampling strategy is illustrated here. As we approach the optima, an accurate estimate of the objective function is made. The two design parameters that are considered for the optimization are also shown in the figure. The top cross-section becomes more tapered and aligns to reduce the wind effects on the building. The tapering of the cross-section is found to reduce the wind loading. The Twisting is not prominent as the tapering. However, they also converge with the optimization steps.

The risk-averse candidate design is shown in 15. The improvement in the objective function is illustrated in the figure. The objective function improves by 15%. The reduction is more compared to the mean optimization problem presented earlier. The number of samples at each of the optimization steps also increases with optimization steps. When compared to the mean optimization problem, the number of samples is almost three times. This is expected as more samples are required to estimate the tail of the objective function. The shape change in the two objective functions is more than that of the mean optimization problem. The QoI is clearly not symmetrical, and hence a mean and std, which is a symmetric measure of the risk, may not best the idea for such a problem.

The optimization results clearly indicate that the twisting and tapering are efficient strategies for reducing the wind effects on the structure. Also, the effect of uncertainties is considered during the optimization procedure. The optimization strategies presented in deliverable 6.5[7] are demonstrated for the wind flow problem.

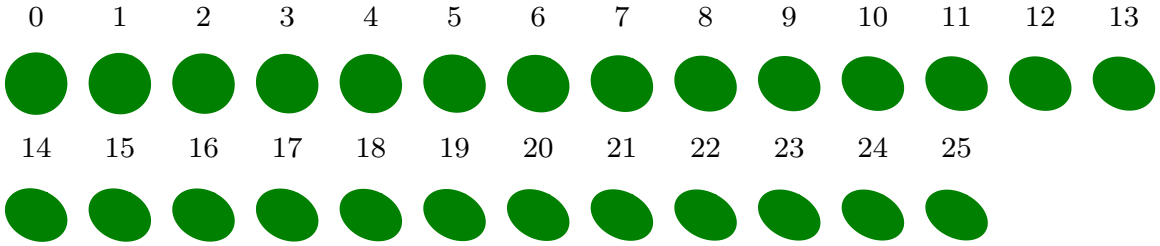

(a) Mean optimization

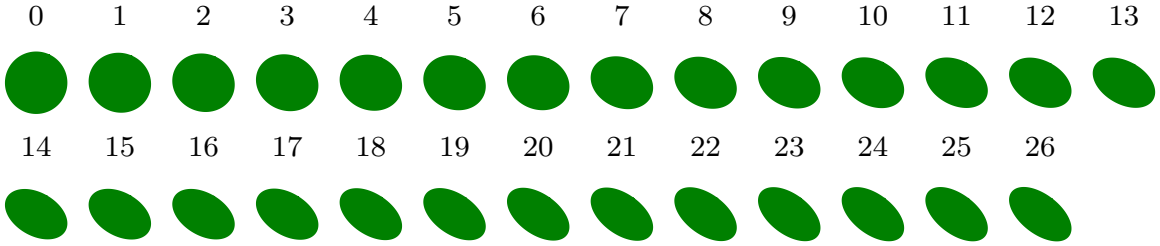

(b) CVaR optimization.

Figure 13: Shape at the top of the building for each optimization steps.

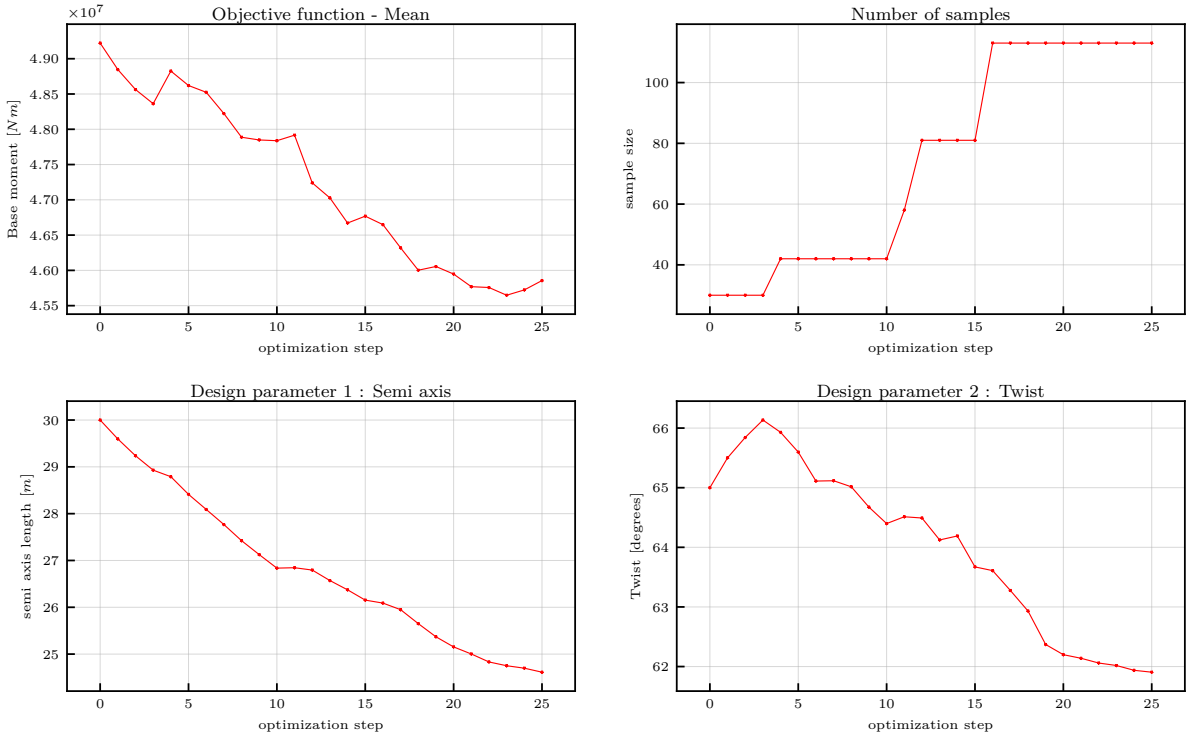

Figure 14: Progress of Mean optimization

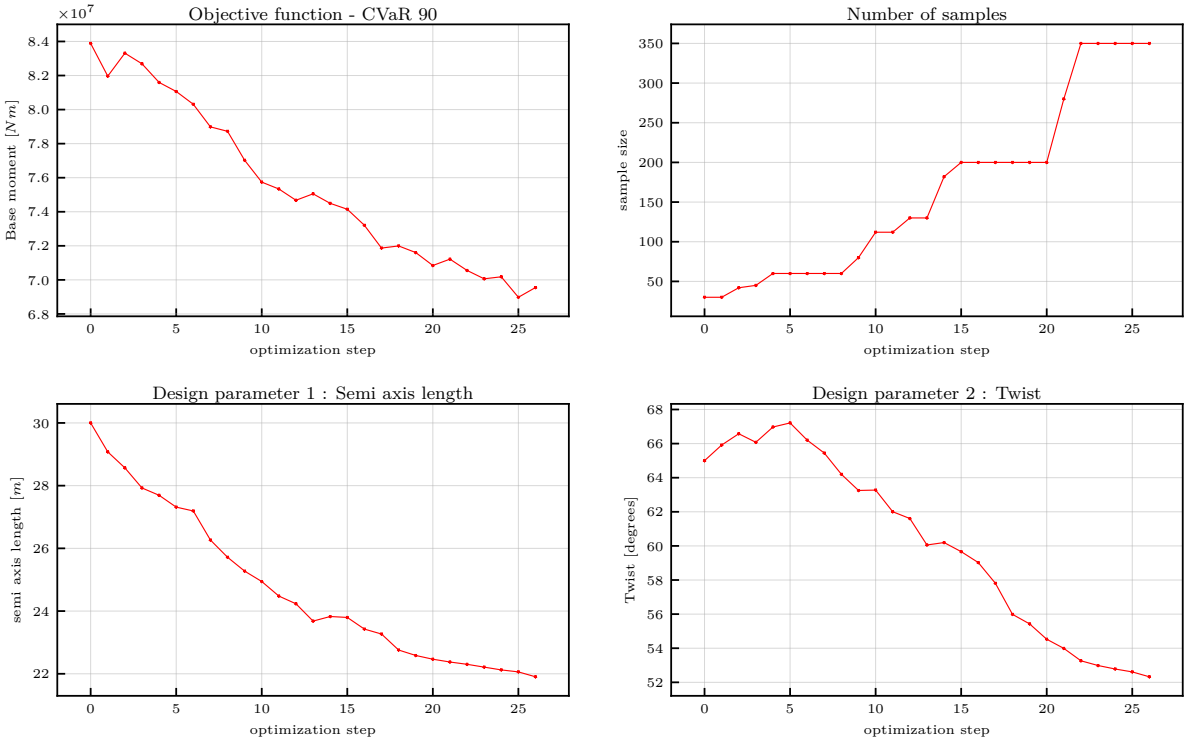

Figure 15: Progress of CVaR optimization

4 Engineering Evaluation of OUU results

The stochastic optimization of the tapered and twisted tower explicitly prove the applicability of the developed methods of the ExaQUte project and, in particular, the Workpackages 6 and 7. From an engineering and architectural point of view, the depicted OUU workflow, compare Figure 11, is especially suited to be integrated into preliminary design studies and early planning stages, where main decisions regarding the building's shape and primary load bearing structure are defined (integration of the OUU workflow at str.ucture GmbH is part of the exploitation plan, cf. Deliverable 8.4).

A very promising perspective for the application of the OUU strategy is also given in later stages of the design and construction process, especially for tall high-rise buildings. Local shape changes, e. g. including openings or corner modifications within a chosen curved facade system, cf. [8], that have a major impact on the wind loads, can thereby be determined such that these wind loads are reduced. It should again be noted, that due to the incorporation of the stochastic approach that includes uncertain wind fields, the developed methodology is superior to existing commercial shape optimization tools, that primarily treat shape optimization for single, in most cases static load cases.

Looking at a wider context, there are numerous fields, where the stochastic optimization results can play an important role. A key area is given in modern data-based urban planning. Due to the rising availability of local climate and wind data in and around cities, urban planers and decision takers are increasingly interested in modelling techniques that predict varying wind flow and temperature conditions within urban areas. Interests lie in the microclimate evaluation in early preliminary urban planning but also during redensification measures in densely populated areas.

A transfer of the stochastic shape optimization technique towards optimising e. g. steady wind flow in zones for fresh air supply while varying the building's height as optimisation parameters poses an interesting future field of application, where the derived derivations and hypotheses still hold for the highly uncertain conditions. Furthermore, the optimised data-driven wind field generation enables the consideration of local wind data into the simulation environment and is a key aspect for the acceptance and the permanent adoption of computer-aided wind engineering in local communities and stakeholders.

References

[1] *EN 1991-1-4 Actions on structures - Wind*, volume 4. 2011.

[2] M. Andre, M. Mier-Torrecilla, and R. Wüchner. Numerical simulation of wind loads on a parabolic trough solar collector using lattice Boltzmann and finite element methods. *Journal of Wind Engineering and Industrial Aerodynamics*, 146: 185–194, 2015. ISSN 01676105. doi:10.1016/j.jweia.2015.08.010. URL `http://dx.doi.org/10.1016/j.jweia.2015.08.010`.

[3] M. Andre, M. Peentek, K.-U. Bletzinger, and R. Wuechner. Aeroelastic simulation of the wind-excited torsional vibration of a parabolic trough solar collector. *Journal of Wind Engineering and Industrial Aerodynamics*, 165:67–78, 2017. doi:10.1016/j.jweia.2017.03.005.

[4] ASCE 7-98. *Minimum design loads for buildings and other structures*. 2002. ISBN 0784406243.

[5] M. Asghari Mooneghi and R. Kargarmoakhar. Aerodynamic Mitigation and Shape Optimization of Buildings: Review. *Journal of Building Engineering*, 6:225–235, 2016. ISSN 23527102. doi:10.1016/j.jobe.2016.01.009. URL `http://dx.doi.org/10.1016/j.jobe.2016.01.009`.

[6] Q. Ayoul-Guilmard, F. Nobile, S. Ganesh, M. Núñez, A. Kodakkal, R. Rossi, and C. Soriano. D6.4 Report on stochastic optimisation for unsteady problems. Technical report, Open Access Repository of the ExaQUte project: Deliverables, 2020. URL `https://doi.org/10.23967/exaqute.2021.2.003`.

[7] Q. Ayoul-Guilmard, F. Nobile, S. Ganesh, M. Núñez, A. Kodakkal, R. Rossi, and C. Soriano. D6.5 Report on stochastic optimization for wind engineering. Technical report, Open Access Repository of the ExaQUte project: Deliverables, 2021.

[8] Q. Ayoul-Guilmard, F. Nobile, S. Ganesh, M. Nuñez, A. Kodakkal, R. Rossi, and C. Soriano. D6. 4 report on stochastic optimisation for unsteady problems. 2021.

[9] R. M. Badia, J. Conejero, C. Diaz, J. Ejarque, D. Lezzi, F. Lordan, C. Ramon-Cortes, and R. Sirvent. {COMP} Superscalar, an interoperable programming framework. *SoftwareX*, 3–4, 2015. doi:10.1016/j.softx.2015.10.004.

[10] S. Bider, U. Khristenko, R. Tosi, R. Rossi, and C. Soriano. D7.3 Report on UQ results and overall user experience. Technical report, Open Access Repository of the ExaQUte project: Deliverables, 2021. URL `https://doi.org/10.23967/exaqute.2021.9.002`.

[11] B. Blocken. 50 years of Computational Wind Engineering: Past, present and future. *Journal of Wind Engineering and Industrial Aerodynamics*, 129:69–102, 2014. ISSN 01676105. doi:10.1016/j.jweia.2014.03.008. URL `http://dx.doi.org/10.1016/j.jweia.2014.03.008`.

[12] R. Bollapragada, R. Byrd, and J. Nocedal. Adaptive sampling strategies for stochastic optimization. *SIAM Journal on Optimization*, 28(4):3312–3343, 2018.

[13] R. H. Byrd, G. M. Chin, J. Nocedal, and Y. Wu. Sample size selection in optimization methods for machine learning. *Mathematical programming*, 134(1):127–155, 2012.

[14] L. Carassale, A. Freda, and M. Marrè-Brunenghi. Experimental investigation on the aerodynamic behavior of square cylinders with rounded corners. *Journal of Fluids and Structures*, 44:195–204, 2014. ISSN 08899746. doi:10.1016/j.jfluidstructs.2013.10.010. URL `http://dx.doi.org/10.1016/j.jfluidstructs.2013.10.010`.

[15] J. A. Carnicero, M. C. Ausín, and M. P. Wiper. Non-parametric copulas for circular–linear and circular–circular data: an application to wind directions. *Stochastic environmental research and risk assessment*, 27(8):1991–2002, 2013.

[16] C. Cartis and K. Scheinberg. Global convergence rate analysis of unconstrained optimization methods based on probabilistic models. *Mathematical Programming*, 169(2):337–375, 2018.

[17] G. Comte-Bellot and S. Corrsin. Simple eulerian time correlation of full-and narrow-band velocity signals in grid-generated, 'isotropic' turbulence. *Journal of fluid mechanics*, 48(2):273–337, 1971.

[18] J. Cotela-Dalmau, R. Rossi, and E. Oñate. A fic-based stabilized finite element formulation for turbulent flows. *Computer Methods in Applied Mechanics and Engineering*, 315, 11 2016. doi:10.1016/j.cma.2016.11.020.

[19] P. Dadvand, R. Rossi, and E. Oñate. An object-oriented environment for developing finite element codes for multi-disciplinary applications. *Archives of computational methods in engineering*, 17(3):253–297, 2010.

[20] R. Dutton and N. Isyumov. Reduction of tall building motion by aerodynamic treatments. *Journal of Wind Engineering and Industrial Aerodynamics*, 36:739 – 747, 1990. ISSN 0167-6105. doi:https://doi.org/10.1016/0167-6105(90)90071-J. URL `http://www.sciencedirect.com/science/article/pii/016761059090071J`.

[21] A. Elshaer. Aerodynamic Optimization and Wind Load Evaluation Framework for Tall Buildings. (February), 2017. ISSN 21951071. doi:10.1002/adom.201500336. URL `http://ir.lib.uwo.ca/etd{%}0Ahttp://ir.lib.uwo.ca/etd/4385`.

[22] A. Elshaer, G. Bitsuamlak, and A. El Damatty. Enhancing wind performance of tall buildings using corner aerodynamic optimization. *Engineering Structures*, 136 (April):133–148, 2017. ISSN 18737323. doi:10.1016/j.engstruct.2017.01.019. URL `http://dx.doi.org/10.1016/j.engstruct.2017.01.019`.

[23] E. García-Portugués, R. M. Crujeiras, and W. González-Manteiga. Exploring wind direction and SO_2 concentration by circular–linear density estimation. *Stochastic Environmental Research and Risk Assessment*, 27(5):1055–1067, 2013.

[24] T. Hida, H.-H. Kuo, J. Potthoff, and L. Streit. *White noise: an infinite dimensional calculus*, volume 253. Springer Science & Business Media, 2013.

[25] W. Hu, K. K. Choi, and H. Cho. Reliability-based design optimization of wind turbine blades for fatigue life under dynamic wind load uncertainty. *Structural and Multidisciplinary Optimization*, 54(4):953–970, 2016. ISSN 16151488. doi:10.1007/s00158-016-1462-x.

[26] J. C. Hunt. A theory of turbulent flow round two-dimensional bluff bodies. *Journal of Fluid Mechanics*, 61(4):625–706, 1973.

[27] J. C. Hunt. Turbulence structure in thermal convection and shear-free boundary layers. *Journal of Fluid Mechanics*, 138:161–184, 1984. ISSN 14697645. doi:10.1017/S0022112084000070.

[28] J. C. Hunt and D. J. Carruthers. Rapid distortion theory and the 'problems' of turbulence. *Journal of Fluid Mechanics*, 212(2):497–532, 1990. ISSN 14697645. doi:10.1017/S0022112090002075.

[29] J. C. Hunt and J. M. Graham. Free-stream turbulence near plane boundaries. *Journal of Fluid Mechanics*, 84(2):209–235, 1978. ISSN 14697645. doi:10.1017/S0022112078000130.

[30] IEC. Wind turbines–Part 1: Design requirements. *International Electrotechnical Commission, Geneva*, 61400-1:2014.

[31] P. A. Irwin. Wind engineering challenges of the new generation of super-tall buildings. *Journal of Wind Engineering and Industrial Aerodynamics*, 97(7-8):328–334, 2009. ISSN 01676105. doi:10.1016/j.jweia.2009.05.001. URL `http://dx.doi.org/10.1016/j.jweia.2009.05.001`.

[32] J. JCSS. Probabilistic model code. *Joint Committee on Structural Safety*, 2001.

[33] J. C. Kaimal and J. J. Finnigan. *Atmospheric boundary layer flows: their structure and measurement*. Oxford university press, 1994.

[34] J. C. Kaimal, J. Wyngaard, Y. Izumi, and O. Coté. Spectral characteristics of surface-layer turbulence. *Quarterly Journal of the Royal Meteorological Society*, 98 (417):563–589, 1972.

[35] A. Kareem and A. Tamura. *Advanced structural wind engineering*. Springer, 2015.

[36] B. Keith, U. Khristenko, and B. Wohlmuth. *Learning the structure of wind: A PyTorch implementation of the deep rapid distortion synthetic turbulence model*, 2021. `http://doi.org/10.5281/zenodo.5076306`.

[37] B. Keith, U. Khristenko, and B. Wohlmuth. A fractional pde model for turbulent velocity fields near solid walls. *Journal of Fluid Mechanics*, 916, 2021.

[38] B. Keith, U. Khristenko, and B. Wohlmuth. Learning the structure of wind: A data-driven nonlocal turbulence model for the atmospheric boundary layer. *Physics of Fluids*, 33(9):095110, 2021.

[39] D. P. Kouri and A. Shapiro. Optimization of PDEs with uncertain inputs. In *Frontiers in PDE-Constrained Optimization*, pages 41–81. Springer, 2018.

[40] H.-H. Kuo. *White noise distribution theory*. CRC press, 2018.

[41] L. Landau and E. Lifshitz. *Fluid mechanics*, volume 6. Pergamon, 1987.

[42] D. J. Lea, M. R. Allen, and T. W. Haine. Sensitivity analysis of the climate of a chaotic system. *Tellus A: Dynamic Meteorology and Oceanography*, 52(5):523–532, 2000.

[43] M. Lesieur. *Turbulence in fluids: Stochastic and numerical modelling*, volume 488. Nijhoff Boston, MA, 1987.

[44] A. Lischke, G. Pang, M. Gulian, F. Song, C. Glusa, X. Zheng, Z. Mao, W. Cai, M. M. Meerschaert, M. Ainsworth, et al. What is the fractional Laplacian? A comparative review with new results. *Journal of Computational Physics*, 404:109009, 2020.

[45] G. J. Lord, C. E. Powell, and T. Shardlow. *An introduction to computational stochastic PDEs*, volume 50. Cambridge University Press, 2014.

[46] F. Lordan, E. Tejedor, J. Ejarque, R. Rafanell, J. Álvarez, F. Marozzo, D. Lezzi, R. Sirvent, D. Talia, and R. M. Badia. ServiceSs: An Interoperable Programming Framework for the Cloud. *Journal of Grid Computing*, 12(1):67–91, 2014. ISSN 15707873. doi:10.1007/s10723-013-9272-5.

[47] J. Mann. The spatial structure of neutral atmospheric surface-layer turbulence. *Journal of fluid mechanics*, 273:141–168, 1994.

[48] J. Mann. Wind field simulation. *Probabilistic engineering mechanics*, 13(4):269–282, 1998.

[49] A. Michalski, P. D. Kermel, E. Haug, R. Löhner, R. Wüchner, and K. U. Bletzinger. Validation of the computational fluid-structure interaction simulation at real-scale tests of a flexible 29m umbrella in natural wind flow. *Journal of Wind Engineering and Industrial Aerodynamics*, 99(4):400–413, 2011. ISSN 01676105. doi:10.1016/j.jweia.2010.12.010.

[50] A. Paszke, S. Gross, F. Massa, A. Lerer, J. Bradbury, G. Chanan, T. Killeen, Z. Lin, N. Gimelshein, L. Antiga, A. Desmaison, A. Kopf, E. Yang, Z. DeVito, M. Raison, A. Tejani, S. Chilamkurthy, B. Steiner, L. Fang, J. Bai, and S. Chintala. PyTorch: An imperative style, high-performance deep learning library. In *Advances in Neural Information Processing Systems 32*, pages 8024–8035. Curran Associates, Inc., 2019. URL `http://papers.neurips.cc/paper/9015-pytorch-an-imperative-style-high-performance-deep-learning-library.pdf`.

[51] M. Peentek, A. Winterstein (geb. Mini), M. Vogl, P. Kupás, K.-U. Bletzinger, and R. Wüchner. A multiply-partitioned methodology for fully-coupled computational wind-structure interaction simulation considering the inclusion of arbitrary added mass dampers. *Journal of Wind Engineering and Industrial Aerodynamics*, 177:117–135, 2018. doi:10.1016/j.jweia.2018.03.010.

[52] S. B. Pope. *Turbulent flows*. IOP Publishing, 2001.

[53] R. T. Rockafellar and J. O. Royset. Engineering decisions under risk averseness. *ASCE-ASME Journal of Risk and Uncertainty in Engineering Systems, Part A: Civil Engineering*, 1(2):04015003, 2015.

[54] R. T. Rockafellar, S. Uryasev, et al. Optimization of conditional value-at-risk. *Journal of risk*, 2:21–42, 2000.

[55] E. Simiu and D. Yeo. *Wind effects on structures: Modern structural design for wind*. John Wiley & Sons, 2019.

[56] G. R. Tabor and M. Baba-Ahmadi. Inlet conditions for large eddy simulation: A review. *Computers & Fluids*, 39(4):553–567, 2010.

[57] E. Tejedor, Y. Becerra, G. Alomar, A. Queralt, R. M. Badia, J. Torres, T. Cortes, and J. Labarta. PyCOMPSs: Parallel computational workflows in Python. *International Journal of High Performance Computing Applications*, 31(1):66–82, 2017. ISSN 17412846. doi:10.1177/1094342015594678.

[58] N. H. Thomas and P. E. Hancock. Grid turbulence near a moving wall. *Journal of Fluid Mechanics*, 82(3):481–496, 1977. ISSN 14697645. doi:10.1017/S0022112077000792.

[59] A. Townsend. *The structure of turbulent shear flow*. Cambridge university press, 1980.

[60] T. Von Karman. Progress in the statistical theory of turbulence. *Proceedings of the National Academy of Sciences of the United States of America*, 34(11):530, 1948.